

Chapter 4

Separating the spectra of faint companions

There many different techniques to disentangle the spectra of binary objects. In this chapter we focus on applying a direct subtraction method to near-infrared (nIR) spectra of FGK stars with Brown Dwarf (BD) companions. The data used was obtained with the CRIRES instrument in 2012 with the purpose to apply this technique specifically. A level of trust was placed in the quality of the observations, which was misplaced. We will begin this chapter with the motivation for these specific targets and detail the observations obtained. We will then present the direct subtraction technique and explore in detail how the observations are insufficient to apply this method, and explore this technique at low RV separations by comparison to simulated results.

4.1 techniques

Binary stars through brown dwarfs... to planets.

Mention the other technique here first. Then move to the one we tried...

4.2 Motivation

Motivation section

Why this technique and not others. - separation of components - direct imaging (cant separate)

Find direct imaging limitations —

4.3 Motivation and target selection

The work of Sahlmann et al. (2011) identified several candidate brown dwarf companions of FGK stars with $M_2 \sin i$ values $> 10 M_{\text{Jup}}$. Seven candidates from Sahlmann et al. (2011), which were visible in Period 89 (2012), were selected for further observation in order to identify their stellar nature. That is, to refine the mass of the companions to distinguish if they companion is a large giant planet ($M \lesssim 13 M_{\text{Jup}}$), a Brown dwarf ($13 \lesssim M \lesssim 80 M_{\text{Jup}}$) or a low-mass star ($M \gtrsim 80 M_{\text{Jup}}$).

The spectral differential approach was chosen with the goal to constrain the companion masses while minimizing the observational time required to observe. It was deemed that it should be possible to

Table 4.1: Stellar parameters of the host stars. V is the apparent magnitude taken from SIMBAD (Wenger et al. 2000). Distances were calculated from the GAIA DR2 parallax measurements.

| Star | SpT | V | T_{eff} (K) | $\log g$ (cm s ⁻²) | [Fe/H] | M_1 (M _⊙) | Age (Gyr) | d (pc) | Ref |
|-----------|-----|------|----------------------|--------------------------------|--------------|-------------------------|------------|--------------|-----|
| HD 4747 | K0V | 7.15 | 5316 ± 50 | 4.48 ± 0.10 | -0.21 ± 0.05 | 0.81 ± 0.02 | 3.3 ± 2.3 | 18.80 ± 0.04 | 1, |
| HD 162020 | K3V | 9.12 | 4723 ± 71 | 4.31 ± 0.18 | -0.10 ± 0.03 | 0.74 ± 0.07 | 3.1 ± 2.7 | 30.85 ± 0.06 | 4, |
| HD 167665 | F9V | 6.40 | 6224 ± 50 | 4.44 ± 0.10 | 0.05 ± 0.06 | 1.14 ± 0.03 | 0.7 – 3.6 | 31.24 ± 0.06 | 5, |
| HD 168443 | G6V | 6.92 | 5617 ± 35 | 4.22 ± 0.05 | 0.06 ± 0.05 | 1.01 ± 0.07 | 10.0 ± 0.3 | 39.67 ± 0.12 | 5, |
| HD 202206 | G6V | 8.07 | 5757 ± 25 | 4.47 ± 0.03 | 0.29 ± 0.02 | 1.04 ± 0.07 | 2.9 ± 1.0 | 46.03 ± 0.14 | 5, |
| HD 211847 | G5V | 8.62 | 5715 ± 24 | 4.49 ± 0.05 | -0.08 ± 0.02 | 0.92 ± 0.07 | 0.1 – 6.0 | 48.81 ± 0.13 | 1, |
| HD 30501 | K2V | 7.59 | 5223 ± 50 | 4.56 ± 0.10 | 0.06 ± 0.06 | 0.81 ± 0.02 | 0.8 – 7.0 | 20.37 ± 0.01 | 1, |

References: (1) Sahlmann et al. (2011); (2) Santos et al. (2005); (3) Crepp et al. (2016); (4) Tsantaki et al. (2013); (5) Lendl et al. (2016); (6) Santos et al. (2004); (7) Sousa et al. (2008); (8) Collaboration et al. (2018);

obtain a detection of a companion at 1% contrast ratio with an exposure time of around 20 minutes. Two observations at “clearly separate RVs” were requested to constrain each target. Observations were performed without telluric standard star observations to avoid the wasted observing time, choosing to instead rely on synthetic model correction (see 3.4.1.1). The *K*-band was chosen to achieve a high contrast relative to the host star, detected in the extreme V-K colour indexes (>7.8).

The list target host stars are presented in Table 4.1 along with their stellar parameters, while the companion orbital parameters are provided in Table 4.2.

We note that the orbital parameters of some targets have been refined in the literature since the observations took place. For example three candidates have had their masses refined in recent works. The companion to HD 211847 was determined to be a low mass star with $M_2 = 155 M_{\text{Jup}}$ (Moutou et al., 2017), while the companion to HD 4747 was found to have a mass of $M_2 = 60 M_{\text{Jup}}$ (Crepp et al., 2016). The two companions of HD 202206 (B and c) were found to have masses of $M_B = 93.6 M_{\text{Jup}}$ and $M_c = 17.9 M_{\text{Jup}}$, respectively, classifying HD 202206c as a “circumbinary brown dwarf” (Benedict and Harrison, 2017). These three **target** with recently refined masses (along with HD 30501) create a good set **benchmarks** to compare any results from the techniques developed here, and show that the masses of these targets do span the BD – low mass star range. All target companions except HD 162020 (P=8.4 days) are in (very) long period orbits (P=0.7–38 years) with masses (or $M_2 \sin i$) greater than 10 M_{Jup} .

Rotate orbital parameter table.

4.3.1 The Data

4.3.2 CRIRES data

Observations were performed with the CRIRES instrument (Kaeufl et al., 2004) configured to observe a narrow wavelength domain of the *K*-band between 2 120–2 160 nm. The slit width of 0.4'' resulted in an instrumental resolving power of $R = 50\,000^1$. No adaptive optics were used to ensure that the entrance slit was entirely covered by each target. This is to prevent strong slit illumination variations that could change the shape of spectral lines.

The observations were performed in service mode during Period 89 with run ID. 089.C-0977(A) between April and August 2012. **An** single observation is composed of eight individual spectra with

¹ The rule of thumb resolution for CRIRES is $100\,000 \frac{0.2''}{\text{slitwidth}}$

Table 4.2: Orbital parameters for the BD companions obtained from the literature. **Yes need rotating.**

| Object | γ (km s ⁻¹) | Period (day) | e | K_1 (m s ⁻¹) | T_0 (JD-2,450,000) | ω (deg) | M (M_J) |
|------------|-----------------------------------|-----------------------|-------------------|-------------------------------|-------------------------|-------------------|------------------|
| HD 4747 | 0.215 ± 11 | $13\,826.2 \pm 314.1$ | 0.740 ± 0.002 | 755.3 ± 12 | 463.1 ± 7.3 | 269.1 ± 0.6 | |
| HD 162020 | -27.328 ± 0.002 | $8.42819 \pm 6e^{-5}$ | 0.277 ± 0.002 | $1\,813 \pm 4$ | $1\,990.68 \pm 0.01$ | 28.4 ± 0.2 | |
| HD 167665 | 8.003 ± 0.008 | $4\,451.8 \pm 27.6$ | 0.340 ± 0.005 | 609.5 ± 3.3 | $6\,987.6 \pm 29$ | -134.3 ± 0.9 | |
| HD 168443b | -0.047 ± 0.552 | $58.1124 \pm 4e^{-4}$ | 0.529 ± 0.001 | 475.13 ± 0.9 | $5\,626.20 \pm 0.02$ | 172.9 ± 0.1 | |
| HD 168443c | -0.047 ± 0.552 | $1\,749.83 \pm 0.57$ | 0.211 ± 0.002 | 297.7 ± 0.6 | $5\,521.3 \pm 2.2$ | 64.9 ± 0.5 | |
| HD 202206B | 14.721 | 256.33 ± 0.02 | 0.432 ± 0.001 | 567 ± 1 | $2\,176.14 \pm 0.12$ | 161.9 ± 0.2 | |
| HD 202206c | 14.721 | $1\,260 \pm 11$ | 0.22 ± 0.03 | 41 ± 1 | $3\,103 \pm 452$ | 280 ± 4 | |
| HD 211847 | 6.689 ^a | $7\,929.4 \pm 2\,500$ | 0.685 ± 0.068 | 291.4 ± 12.2 | $12\,030.1 \pm 2\,500$ | 159.2 ± 2.0 | |
| HD 30501 | 23.710 ± 0.028 | $2\,073.6 \pm 3.0$ | 0.741 ± 0.004 | $1\,703.1 \pm 26.0$ | $3\,851.5 \pm 3.0$ | 70.4 ± 0.7 | |

References. (1) Crepp et al. (2016); (2) Udry et al. (2002); (3) Sahlmann et al. (2011); (4) Pilyavsky et al. (2011); (5) Correia et al. (2005); (6) Benedict and Harrison (2017); (7) Moutou et al. (2017)

Notes. ^(a) fixed

an integration time of 180s each, observed in the ABBAABBA nod cycle pattern to obtain a high signal-to-noise (>100) when combined. The list of observations obtained with CRIRES are provided in Table 4.3.

There is a slight inconsistency with the some of the observations, taken in service mode. For instance HD 202206 has two observations taken with the Ks filter, while one is taken with the J filter. There is also the last observation of HD 30501 taken with a different filter to **to** rest. We are unable to access the phase two proposal to determine if this was requested as such or it was an observational mistake.

There is also **a** inconsistency with the ordering of **th** observations again with HD 202206. The observation that was performed first is labelled as the third in the fits header file.

The target HD 4747 only has one observation. There could be two possible reasons for this, these observations were preformed in service mode as **filler** and there was time to complete it, or only one observation was requested due to the very long orbital period of the target.

Is there a reason for the two different filters?

The filters ... using the Ks and the Hx5e-2 filters. Why use the different filters???

All observations were reduced using the DRACS pipeline (see Section 3.3.3) with artefact corrections applied. **They were each wavelength** calibrated and corrected for telluric lines following Sections 3.4.1 and 3.4.1.1. The spectra were corrected for Earth's barycentric RV using the *helcor* PyAstronomy² function ported from the REDUCE IDL package (see Piskunov and Valenti (2002)). Using the date and coordinates of the targets **this** function calculates the induced RV from the orbital motion of the Earth around the Sun as well as the rotation of the Earth, projected towards the target. This calculated RV is then used to apply the appropriate Doppler shift on each spectrum to correct for the Earth's barycentric motion.

² <https://pyastronomy.readthedocs.io>

I still assume this is a mistake

Check why the ordering number is incorrect for HD202206. If it is correct like this and is numbered incorrectly in the header then we should mention this.

rotate table?

Table 4.3: Details about the each CRIRES observation. The number of artefacts removed in Section 3.3.3.1 as well as the SNR of the combined spectra is provided. The last three columns are the calculated RV of both host and largest companion, from the orbital solution, as well as the RV difference between the two components.

| Object | Obs. # | Start date (yyyy-mm-dd hh:mm:ss) | Filter | Airmass (at start) | Artefacts / 32 | SNR | RV_1 km s^{-1} | RV_2 km s^{-1} | rv_2 km s^{-1} |
|-----------|-----------|-------------------------------------|--------|-----------------------|-------------------|-----|------------------------------|------------------------------|------------------------------|
| HD 4747 | 1 | 2012-07-06 07:36:06 | Ks | 1.25 | 7 | 340 | -0.219 | -0.154 | 0.065 |
| HD 162020 | 1 | 2012-07-04 06:23:22 | Ks | 1.30 | 2 | 127 | -28.760 | 50.785 ^a | 79.545 ^a |
| HD 162020 | 2 | 2012-07-04 06:57:48 | Ks | 1.44 | 2 | 128 | -28.717 | 48.440 ^a | 77.157 ^a |
| HD 167665 | 1 | 2012-07-28 05:00:53 | Hx5e-2 | 1.24 | 7 | 371 | 7.581 | 18.024 ^a | 10.443 ^a |
| HD 167665 | 2 | 2012-07-28 05:37:27 | Hx5e-2 | 1.39 | 4 | 374 | 7.581 | 18.025 ^a | 10.444 ^a |
| HD 167665 | 3 | 2012-08-05 02:54:03 | Hx5e-2 | 1.04 | 4 | 358 | 7.575 | 18.163 ^a | 10.588 ^a |
| HD 168443 | 1 | 2012-08-05 04:29:32 | Ks | 1.31 | 2 | 192 | -0.121 | 50.932 ^{a,b} | 51.053 ^{a,b} |
| HD 168443 | 2 | 2012-08-05 04:58:50 | Ks | 1.47 | 4 | 190 | -0.121 | 51.189 ^{a,b} | 51.310 ^{a,b} |
| HD 202206 | 1 | 2012-07-12 06:54:44 | Ks | 1.01 | 3 | 189 | 14.843 | 12.992 ^b | -1.851 |
| HD 202206 | 2 | 2012-07-13 05:41:40 | J | 1.01 | 3 | 209 | 14.837 | 13.065 ^b | -1.772 |
| HD 202206 | 3 | 2012-07-11 08:29:55 | Ks | 1.15 | 4 | 180 | 14.849 | 12.920 ^b | -1.929 |
| HD 211847 | 1 | 2012-07-06 07:02:57 | Ks | 1.07 | 4 | 272 | 6.613 | 7.171 | 0.558 |
| HD 211847 | 2 | 2012-07-13 06:54:37 | Ks | 1.05 | 5 | 283 | 6.614 | 7.167 | 0.553 |
| HD 30501 | 1 | 2012-04-07 00:08:29 | Hx5e-2 | 1.60 | 3 | 217 | 22.372 | 36.377 | 14.005 |
| HD 30501 | 2 | 2012-08-01 09:17:30 | Hx5e-2 | 1.42 | 10 | 212 | 22.505 | 35.120 | 12.615 |
| HD 30501 | 3 | 2012-08-02 08:47:30 | Hx5e-2 | 1.53 | 8 | 237 | 22.507 | 35.102 | 12.595 |
| HD 30501 | 4 | 2012-08-06 09:42:07 | Ks | 1.28 | 7 | 235 | 22.514 | 35.031 | 12.517 |

^a Maximum RV given $M_2 \sin i$ only.

^b Largest mass companion only.

4.3.3 Calculations using observed times

Before the differential subtraction method is presented, calculations can be preformed to estimate the RV of both components in each observations and the likely separation between the companions between observations. The time of each observation is combined with the orbital parameters from Table 4.2 and Equation ?? to calculate the RV of the host star (RV_1 in 4.3). For the companion the mass or $M_2 \sin i$ is used alongside the stellar mass from possible from Table ?? to calculate the RV of the companion using Equation ?? (RV_2 in 4.3). The difference in RV between the host **an** companion **each** observation is also computed as $rv_2 = RV_2 - RV_1$ although it will not be used until 5.

The magnitude of the RV separation of the two companion spectra in the differential ΔRV is calculated following Equation 4.5 and provided in 4.4. this table also contains the estimated semi-major RV amplitude for the companion K_2 and the phase coverage from the observations. The phase coverage is the fraction of the orbit covered between the observations for each target. For HD 4747 the ΔRV and phase coverage values are missing due to **a** single observation.

The full orbital solution for the components along with the times of observations are provided later in Section 4.5.

I am not sure if this is the best location for this section.

equations for companion rv with the masses still included. include 180 degree angle phase change also

Fix caption position here

recalculate values that are less than 1

Table 4.4: Estimated orbital semi-amplitude and RV separation of the companion, given the companion mass (M_2 or $M_2 \sin i$) from Table 4.2 and observation times from Table 4.3.

| Companion | Estimated K_2 (km s^{-1}) | Estimated $ \Delta RV $ (m s^{-1}) | Phase coverage (%) |
|------------|--|---|-----------------------|
| HD 4747 | -10.65 | — | — |
| HD 162020 | -98.92 ^a | 2 388 | 0.28 |
| HD 167665 | -14.47 ^a | 145 | 0.18 |
| HD 168443b | -64.65 ^a | 258 | 0.035 |
| HD 168443c | -18.05 ^a | <1 | 0.001 |
| HD 202206B | -6.79 | 78 | 0.74 |
| HD 202206c | -2.50 | <1 | 0.15 |
| HD 211847B | -1.85 | 5 | 0.09 |
| HD 30501 | -16.12 | 1 410 | 5.8 |

^a Maximum K_2 only given $M_2 \sin i$

4.4 Direct Subtraction Method

Here we present the direct subtraction method used, which is similar to previous works (Ferluga et al., 1997; Kostogryz et al., 2013). Assuming that the instrumental profile and atmospheric absorption are dealt with appropriately the spectra of the observed targets are assumed to be composed of two components. A bright host star blended with the faint companion. The spectrum received from the host-companion pair is given by the superposition of two spectral components (J_1 , J_2):

$$I(\lambda) = J_1(\lambda - v_1) + J_2(\lambda - v_2) \quad (4.1)$$

where the subscripts 1 and 2 indicate the spectrum of the host and companion respectively, and λ represents the wavelength of the spectra and $\lambda - v$ represents the Doppler shift $\lambda(1 - v/c)$ by a velocity v .

This can be shifted into the rest frame of the host star by applying the shift v_1 :

$$I(\lambda + v_1) = J_1(\lambda) + J_2(\lambda - v_2 + v_1) \quad (4.2)$$

To analyse J_2 , the spectral component of interest, the component from the host needs to be carefully removed. If two observations of the same target are observed, denoted with subscripts a and b , there will be relative motion between the components due to the orbit. Assuming that the stellar spectra do not change over time ($J_{1a} = J_{2a}$) and each spectrum can be individually Doppler shifted to the rest frame of the host star $J_1\lambda$, then the spectrum of the host star (J_1) can be removed through subtraction of the two observations. Mutually cancelling the host component while leaving two components of the companion, with a relative Doppler shift between them.

$$\begin{aligned}
S(\lambda) &= I_a(\lambda + v_{1a}) - I_b(\lambda + v_{1b}) \\
&= (J_{1a} + J_{2a}(\lambda - v_{2a} + v_{1a})) - (J_{2b} + J_{2b}(\lambda - v_{2b} + v_{1b})) \\
&= J_{2a}(\lambda - v_{2a} + v_{1a}) - J_{2b}(\lambda - v_{2b} + v_{1b}) \\
S(\lambda + v_{2a} - v_{1a}) &= J_{2a}(\lambda) - J_{2b}(\lambda - v_{2b} - v_{1a} + v_{1b} + v_{2a}) \tag{4.3}
\end{aligned}$$

$$S(\lambda') = J_{2a}(\lambda) - J_{2b}(\lambda - \Delta RV_2) \tag{4.4}$$

where,

$$\Delta RV_2 = v_{1a} - v_{1b} - v_{2a} + v_{2b} \tag{4.5}$$

is the RV difference between the two companion spectral components when the host components are mutually subtracted. and $\lambda' = \lambda + v_{2a} - v_{1a}$

The resulting differential spectra $S\lambda'$, dubbed *s-profile* by Ferluga et al. (1997), is composed of just the companion spectra, shifted and subtracted from itself.

Ferluga et al. (1997) even provide a analytical form for the *s-profile* given a single Gaussian line of the form $J(\lambda) = 1 - D \cdot \exp^{-\pi(\lambda - \lambda_0)^2/W^2}$: ...

$$S(\lambda) = 2D \cdot \exp^{-\pi D^2[(\lambda - \lambda_0)^2 + (k/2)^2]/W^2} \cdot \sinh \frac{\pi D^2(\lambda - \lambda_0)k}{W^2}, \tag{4.6}$$

where λ_0 , D , and W are the central wavelength, depth and equivalent width of the Gaussian line, and $k = \Delta RV_2$ is the shift between the two companion spectra.

From binary dynamics (e.g., Murray and Correia, 2010) the RV amplitudes of the host and companion are related through the mass ratio, q , while having an opposite sign³:

$$v_2 = -q * v_1 \tag{4.7}$$

We can simplify Equation 4.5 by expressing it in terms of the mass ratio and host RV only:

$$\begin{aligned}
\Delta RV_2 &= qv_{1a} - qv_{1b} + v_{1a} - v_{1b} \\
&= (1 + q)(v_{1a} - v_{1b}). \tag{4.8}
\end{aligned}$$

If the ΔRV_2 between the companion spectra is able to be derived from the s-profile (see Ferluga et al., 1997) then the mass ratio of the system, q , can be determined, thereby constraining the mass of the companion.

The values v_{1a} and v_{1b} are radial velocity of the host components. The values we use were calculated using the RV equation 2.1 using the orbital parameters from the literature and provided in 4.2 and are used to shift each spectra to the hosts rest frame. These components can also be determined directly from the spectrum by cross-correlating the observed spectrum with a stellar template of the host and were in reasonable agreement. The same values were already used to shift and mutually cancel the host spectrum.

³ The opposite sign arises from a 180° difference in the angle of periaapsis, ω , for the companion.

put in advanced concepts chapter???

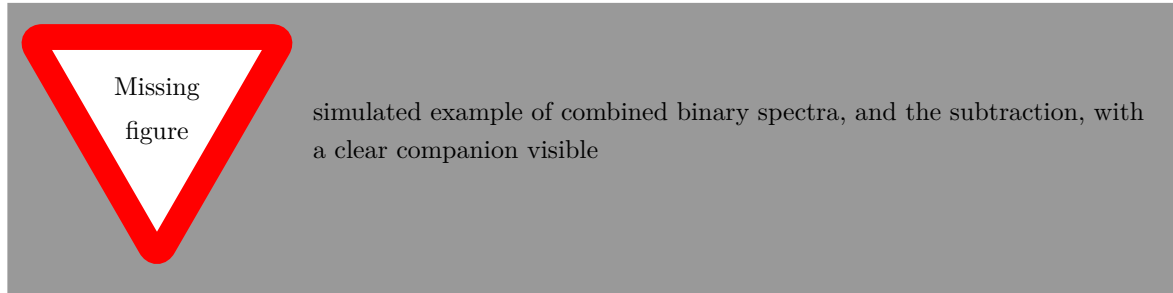
this ignores γ

There should be checks for consistency between v_{1a} , v_{1b} and how well the host component is removed in the s-profile.

If v_{1a} and v_{1b} are incorrect what will happen to q ?

put elsewhere: Equation 4.7 was used to calculate the expected companion RV for each observation in Table 4.3.

Example simulations?



kostov.. 2013 use a very similar method, choosing two observations from the extrema. They also preform a number of simulations regarding observing CRIRES spectra with different brown dwarfs. Figure our the flux ratio limit they get too???

4.4.1 Results of spectral differential analysis

We applied the spectral differential procedure outlined above on the wavelength-calibrated and telluric-corrected CRIRES observations. The spectra were first Doppler shifted to the rest frame velocity of the system by applying a shift of $-\gamma$. The differential subtraction method was then applied by shifting each spectra so that the host lines were at rest and then subtracting one from the other as described above.

It is necessary to have a consistent instrumental setup [Furluga et al. \(1997\)](#), to avoid introducing extra instrumental effects (e.g. slit-width and/or filters) into the spectral differentials and to always observe the same wavelength range and maximize the information to be extracted. In our case, the second observation of HD 202206 and fourth of HD 30501 were taken with different filters compared to the other observations. Therefore, these two observations could not be used for this differential analysis. As noted in [\(Hadrava, 2009\)](#), any spectral differences in the filters would add extra unknown signal/noise making it harder to disentangle the faint spectral differences.

We performed the differential analysis for all targets but only show our most favourable case here, HD 30501, because it is the second largest companion in our sample at $90 M_{\text{Jup}}$ and also has the second largest RV separation between observations. The differential spectra recovered for HD 30501 is shown at the bottom panel of Figure 4.1. The presence of deep ($> 4\%$) stellar and telluric lines in the original spectrum is shaded by the blue and green regions respectively. This indicates that the features of the differential spectrum near these shaded regions are likely due to imperfect telluric correction and host mutual cancellation.

The mutual cancellation of the stellar host works well for the $\sim 40\%$ deep line near 2117 nm , being completely removed, but it does not do so well for the smaller $\sim 10\%$ deep line around 2121.5 nm . The residual for the large $\sim 40\%$ deep telluric line near 2118.5 nm is quite prominent. There is also a wider residual due to three neighbouring lines $\sim 10\%$ deep around 2120 nm which cause features in the differential spectrum. One possible explanation is that the continuum normalization near 2120 nm was influenced by this grouping of lines.

To understand the observed differential signal we simulated a differential spectrum of HD 30501 using a synthetic PHOENIX-ACES spectra with parameters $T_{\text{eff}} = 2\,500\text{ K}$, $\text{textrm{logg}}=5.0$, and $[\text{Fe}/\text{H}]=0.0$, with a RV offset estimated from the observation times. These parameters represent an estimated companion T_{eff} with the metallicity and $\text{textrm{logg}}$ similar to the host (closest grid model). The model spectra were convolved to $R = 50\,000$, continuum normalized and scaled by the estimated flux ratio of the companion. We do not include any synthetic host or telluric spectra and as such simulate the differential result of a “perfect” host cancellation with no telluric contamination present. This is the ideal-case scenario, and we stress that it is impossible to simulate the effect of improper telluric correction in a meaningful way. When comparing the simulated and observed differential in the bottom panel of Figure 4.1, there is a striking amplitude difference. The orange-dashed line of the simulated differential spectrum amplitude is of a much smaller scale than the observed differential. This demonstrates that the amplitude of the differential signal we are trying to detect is much smaller than the residuals created by this differential technique.

The amplitude of the differential signal is lower than we expected due to the very low ΔRV between the observation pairs. The maximum ΔRV between observation pairs, for the observations investigated in this work, are provided in Table 4.4. **There is no ΔRV for HD 4747 as there was only a single observation. We also provide the phase coverage for our targets. We calculate this as the ratio of time between the observed pairs and the orbital period, and show that the fraction of the orbit covered is very small,** all except one covering less than 1 percent of the orbit.

In our best case, HD 30501, the ΔRV of the companion between observations is 1.41 km s^{-1} . For comparison, a single Gaussian absorption line, to be shifted by $\Delta\lambda = \text{FWHM}$ would need a ΔRV of $v_{\text{FWHM}} = c/R = \sim 6\text{ km s}^{-1}$. Since the ΔRV are shifted by a smaller value than the FWHM, the spectral lines of the reconstruction mutually cancel themselves, diminishing the amplitude of the differential signal significantly. As the companion spectra are already faint (with a flux ratio at the percent level) the differential signal is not detectable within these observations and noise level.

When the ΔRV of the companion is smaller than the FWHM of a line there is a mutual subtraction of the companion spectra, diminishing the detected amplitude of the differential signal, and removing the ability to detect the companions using this method. Observations need to be spaced further apart in time/phase to achieve a larger ΔRV separation and increase the amplitude of the differential. Of course once there is a separation there will be complex interactions between neighbouring lines that need to be accounted for.

Since the amplitude is so small **and the** we did not attempt to pursue this further.. We did not attempt the binary reconstruction from the combination...

Ferluga et al. (1997) present a reconstruction method to recover the secondary **y** from the s-profile. Unfortunately **e** this was not appropriate due to insufficient separation.

4.5 Orbital Solutions

The insufficient spacing becomes clear when the RV variation during the orbits are visualized. Figures 4.2–4.10 show the RV curves for each target analysed here. Stars with two companions are shown twice, with each companion treated as a single Keplerian (ignoring the presence of the other companion). **For each** panel on the left hand plot shows the RV variation across a full orbit of the companion, while the panel on the right shows the RV variation for the observation window of Period 89 only (6 months). The solid

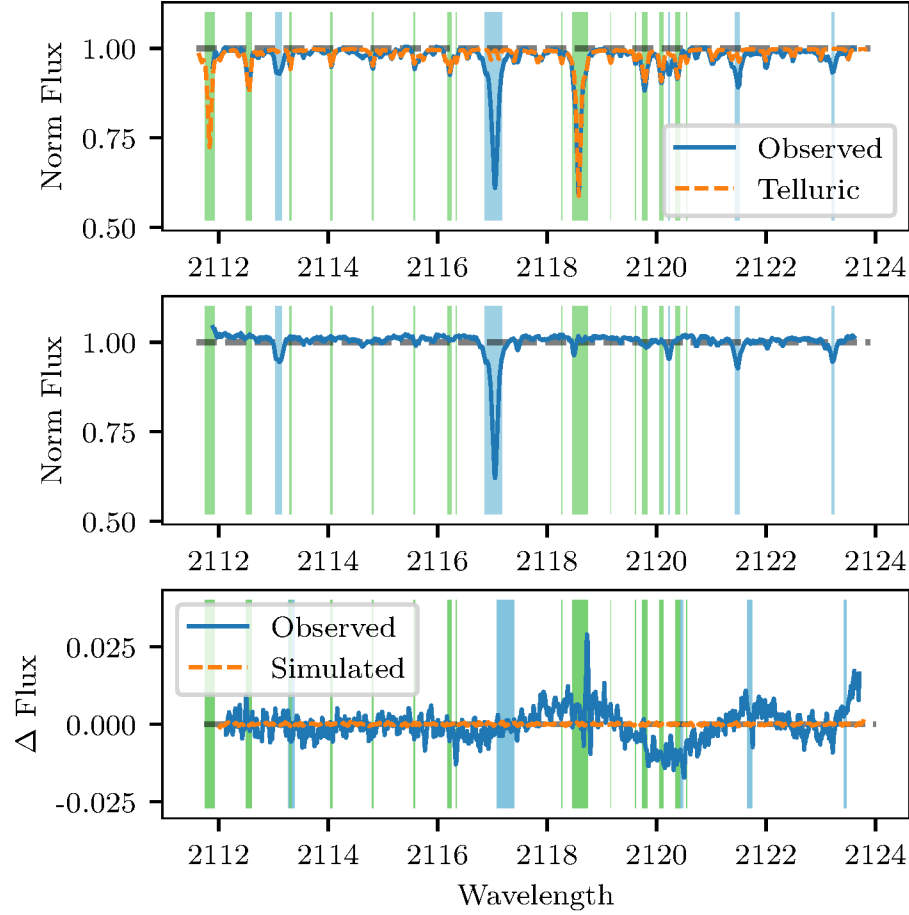


Figure 4.1: (Top) A reduced CRIRES observation of HD 30501 (blue) for detector 1 between 2112–2124 nm along with the tapas telluric absorption model (orange dashed) used for the wavelength calibration and telluric correction. (Middle) The telluric corrected spectra. (Bottom) (blue) Differential spectra for HD 30501 between observations 1 and 3. (orange dashed) Simulated “perfect” differential using PHOENIX-ACES spectra with parameters $T_{\text{eff}} = 2500$ K, $\text{textrm{logg}}=5.0$, and $[\text{Fe}/\text{H}]=0.0$, with the same ΔRV as the observations. The shaded regions indicate where the telluric green and host star blue spectra are $> 4\%$ deep.

black line indicates the RV of the host star (with scale on the left hand axis), while the blue dashed line shows the RV of the companion (with the scale on the right hand axis). The orange crosses and red stars indicate the times at which observations were obtained for each target, for the host and companion respectively.

The first observation easily observed is that RV curves come in many different flavours(shapes). This variations in shape arise from the different orbital parameters of each target (provided in Table 4.2). In the left hand plots, in which a full cycle is shown the different shapes are created from the eccentricity, e , and argument of periapsis, ω . In the right hand panels for which a fixed time period is shown the parameter affecting the image shown is the orbital period of the companion. Specifically the ratio of Period 89 to the orbital period determines what fraction (or multiples) of the orbit to display.

The RV curves of the star and the planet mirror each other about the systems mean velocity γ , with the amplitude scaled by their mass ratio (see Equation ?? advanced topics for q).

All the plots apart from HD 4747 have more than one observations indicated but this is difficult to tell as they are nearly all on top of each other.

For the companions HD 162020b (Figure ??) and HD 168443b (Figure 4.5) their orbital periods are shorter than 6 months, allowing for multiple cycles during Period 89. As such the full amplitude range was available to measure if observations were taken at the locations of the extrema and it should have been possible to obtain observations in which the companion spectra were separated by more than their line FWHM. However the two observations for these two targets were taken immediately after each other. Making any differential extremely small. This is of course ignoring the fact that the flux ratios for these short period companions are estimated to be very low, meaning they would be very difficult to detect if sampled correctly.

The larger companion HD 168443c in Figure 4.6 the orbital period is longer, so they appear as straight lines in the right hand panel. Although the amplitude variation of the companion during Period 89 is about $8\text{--}9\text{ km s}^{-1}$. Therefore observations taken at the extreme ends of Period 89 may have provided just enough separation to obtain a detection.

For HD 202206 about 3/4 of the orbit is covered in Period 89 with a RV amplitude of the companion possible of over 40 km s^{-1} . Therefore, in this case well separated RVs could have been obtained.

For the remain targets it is clear that sufficiently separated RVs were not obtained, but also that they were not possible from a single observing period with less than 6 km s^{-1} variation over Period 89. For HD 30501 in which there was a large time separation between observations was obtained, and is clearly visible in Figure 4.10. Unfortunately this did not result in a large enough companion separation. If the observations had been obtained in the previous period (88) instead then sufficient separation could have been obtained due to the orbital eccentricity. (this region is due to return in ...

The code used to create orbital plots similar to those shown here is available under the iastro-pt/Observationtools⁴ Github repository with documentation available on <https://ia-observationtools.readthedocs.io/en/latest/>

The sampling of points in the orbit reveal that the choice of points was not favourable for the application of the direct subtraction technique. This was however only discovered after attempting to apply the technique.

⁴ <https://github.com/iastro-pt/ObservationTools>

Should I predict when the best time to observe these targets are is? e.g. in 2020 x and x will have sufficient RV change in one period to achieve a detection.

change RV scale for hd4747 orbit

Fix plot titles

Check M2sini labels - can we get M2 only for those that we know

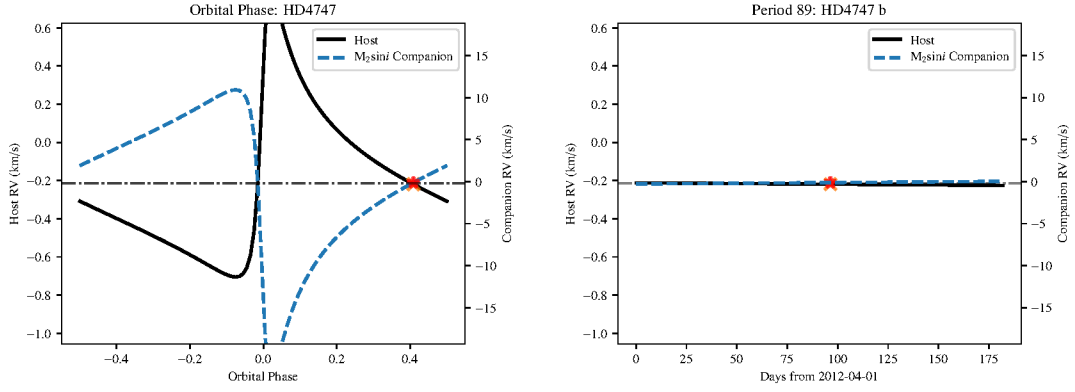


Figure 4.2: RV orbital single companion Keplerian for the HD 4747. The left hand plot shows the RV curve for one full orbit while the right hand panel shows the RV curve over 6 months (Period 89). The solid black line indicates the RV of the host star (with scale on the left), while the blue dashed line indicates the RV of the companion (with scale on the right). The orange crosses and red stars indicate the times at which observations were obtained for the target, for the host and companion respectively.

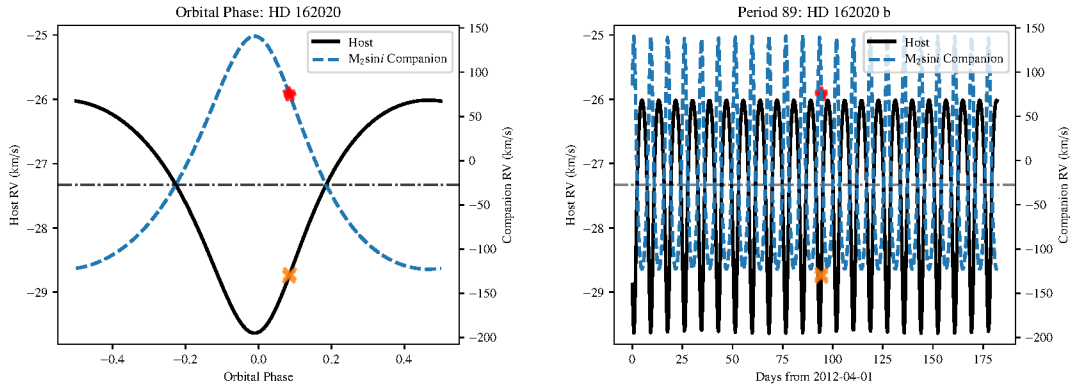


Figure 4.3: Same as Figure 4.2 but for HD 162020.

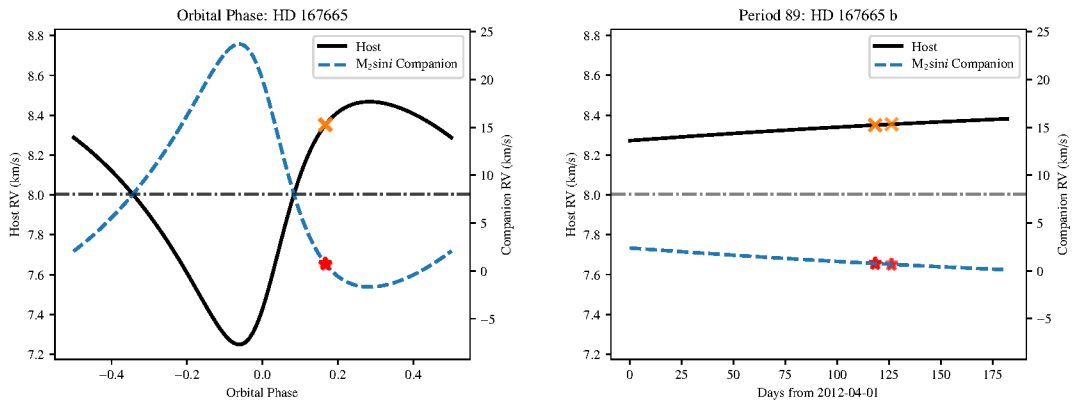


Figure 4.4: Same as Figure 4.2 but for HD 167665.

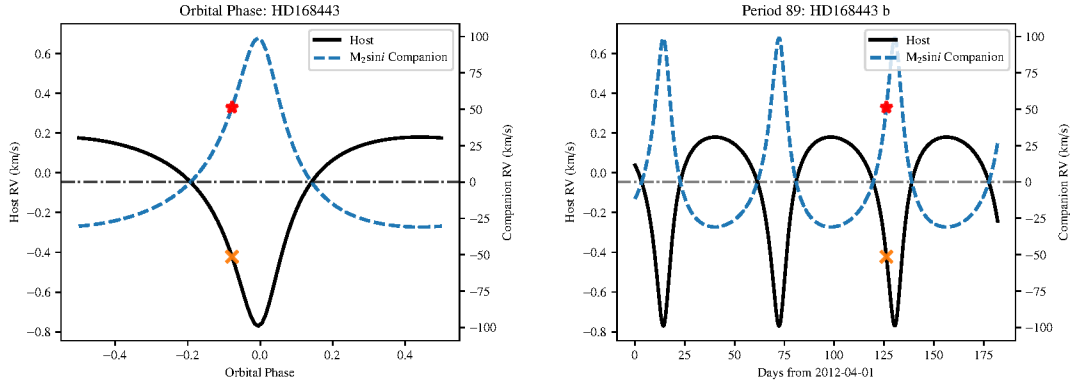


Figure 4.5: Same as Figure 4.2 but for HD 168443b. Analysed as if this was a single companion.

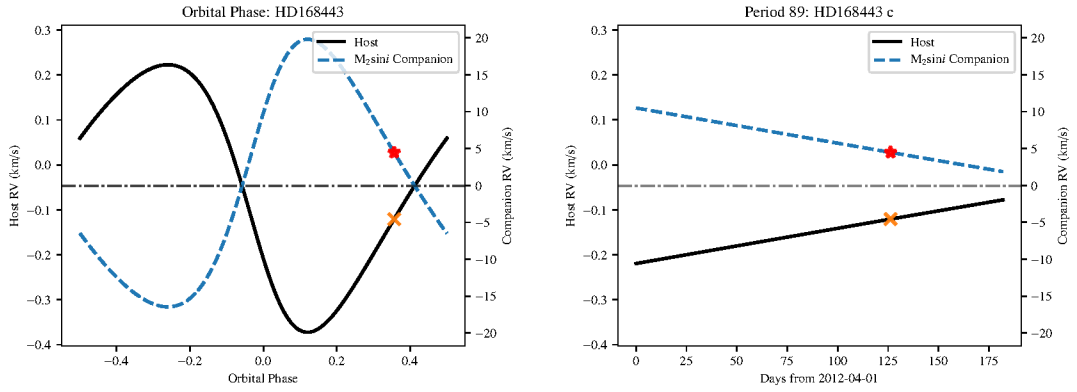


Figure 4.6: Same as Figure 4.2 but for HD 168443c. Analysed as if this was a single companion.

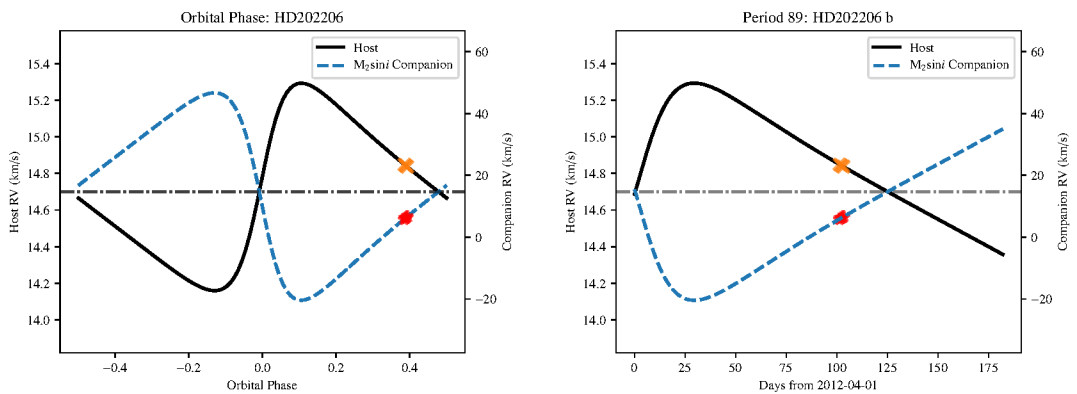


Figure 4.7: Same as Figure 4.2 but for HD 202206B. Analysed as if this was a single companion.

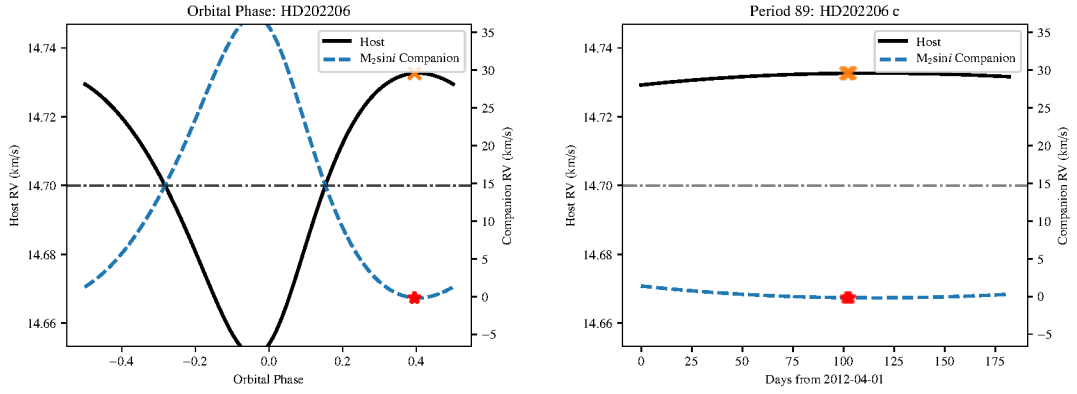


Figure 4.8: Same as Figure 4.2 but for HD 202206c. Analysed as if this was a single companion.

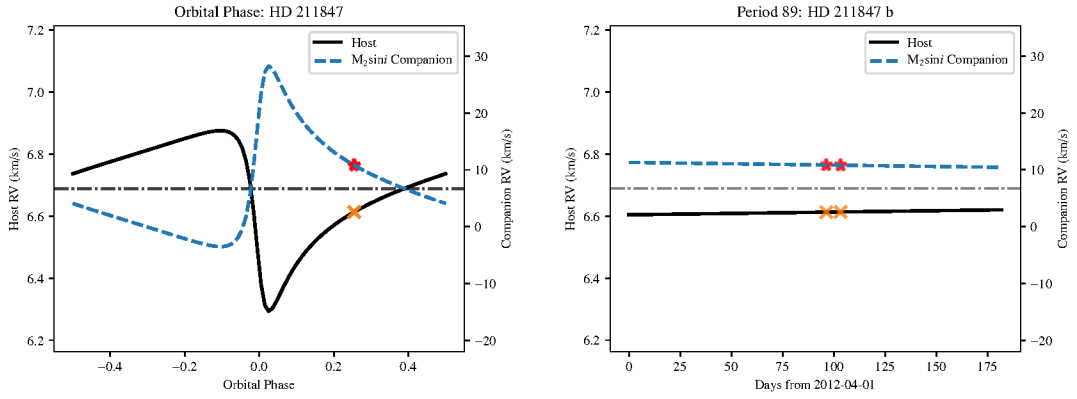


Figure 4.9: Same as Figure 4.2 but for HD 211847.

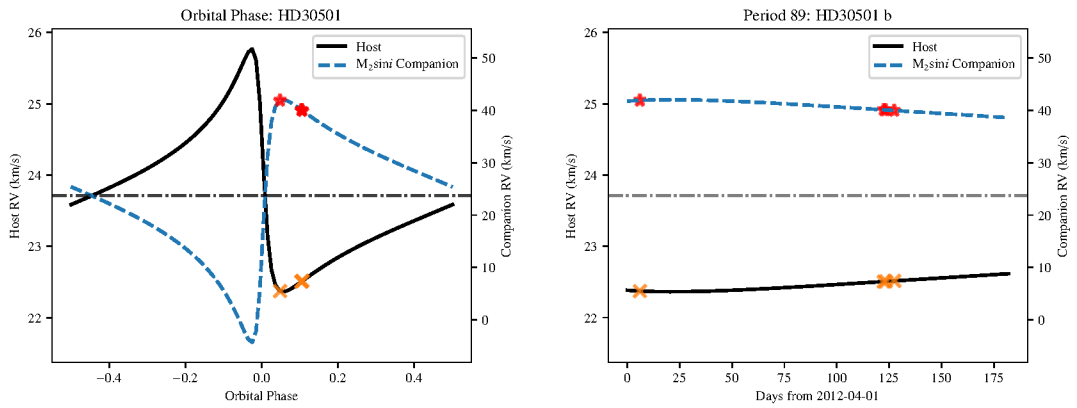


Figure 4.10: Same as Figure 4.2 but for HD 30501.

Should RV of companion be scale by $m_2 \sin i$ only or m_2 if known?

4.5.1 Relative differential amplitude

To investigate the differential subtraction under tiny ΔRV further the change in differential amplitude against variation in RV was explored. Simulations were performed creating a differential spectra for a range of ΔRV s between $\pm 10 \text{ km s}^{-1}$ using the same PHOENIX-ACES spectra for the companion of HD 30501 ($T_{\text{eff}} = 2500 \text{ K}$, $\text{textrm{log}g}=5.0$, $[\text{Fe}/\text{H}]=0.0$) convolved to $R = 50\,000$. These simulations were focused between the wavelength range 2110–2123 nm, corresponding to detector 1 of the CRILES observations. The differential spectra was created for each by taking the synthetic spectrum for the companion, Doppler shifting a copy of the spectrum and subtracting it from the original. At each RV step the maximum absolute differential amplitude (peak to peak) of the simulated differential spectrum observed was recorded. Again these simulations are performed assuming perfect telluric correction and removal of the host star by only considering the spectrum of the companion alone.

The result of this simulation is given in Figure 4.11. As this absolute amplitude is specific to the lines present in the analysed wavelength range, the values were normalized by the median amplitude value outside of the line FWHM (dashed vertical lines), between $\pm(7 - 10) \text{ km s}^{-1}$, to give a relative differential amplitude, independent from the depth of a specific line. Differential subtraction simulations we also performed using a spectrum made up of a single Gaussian line and a single Lorentzian, these are shown in Figure 4.11 as the orange dashed and green dash-dotted lines respectively. The spectral profile shape of differential for the Gaussian line was also checked for consistency with the analytical form of the differential spectra (Ferluga et al. (1997, Equation A.1) (included above as Equation 4.6).

Figure 4.11 that a ΔRV of zero between companion spectra, the spectral lines of the companion completely cancel each other out, resulting in zero amplitude. As the RV separation increases in either direction, the individual lines begin separating, and stop cancelling themselves out. A maximum differential amplitude is achieved when the individual lines are fully separated. We did not consider the shape/width of the differential spectral lobes as done in Ferluga et al. (1997, eqn. A.1), but this could also have been measured.

In the simulations of the synthetic spectrum (and of course real spectra) neighbouring spectral lines begin to strongly interfere, leading to a variable measured relative amplitude beyond 10 km/s . The shape of the relative amplitude becomes complicated due to the interaction but since the ΔRV for all the observations fall well short of this region it was not investigated further. It is suspected that the interaction of neighbouring lines is one possible cause for the difference in the relative differential amplitude between the single theoretical line profiles and synthetic spectrum between 2 and 6 km s^{-1} .

The vertical dotted lines indicate the line $\text{FWHM} = \lambda/R = v/c \text{ velocity}$ of 6 km s^{-1} at $2 \mu\text{m}$ with $R=50\,000$, showing that the amplitude is almost maximum when the lines are separated beyond their line width. The two solid vertical lines in Figure 4.11 indicate the $\Delta RV=1.41 \text{ km s}^{-1}$ separation calculated for our best target, HD 30501 from Table 4.4, given known orbital parameters and the observation times. This shows that our differentials have severely reduced amplitude, $< 20\%$ relative to well separated individual lines. As the companion spectra are already faint and in combination with a host star at $>1\%$ flux ratio the $>80\%$ extra reduction in signal amplitude makes this detection impossible with these observations.

Increase size of diff amp plots to two

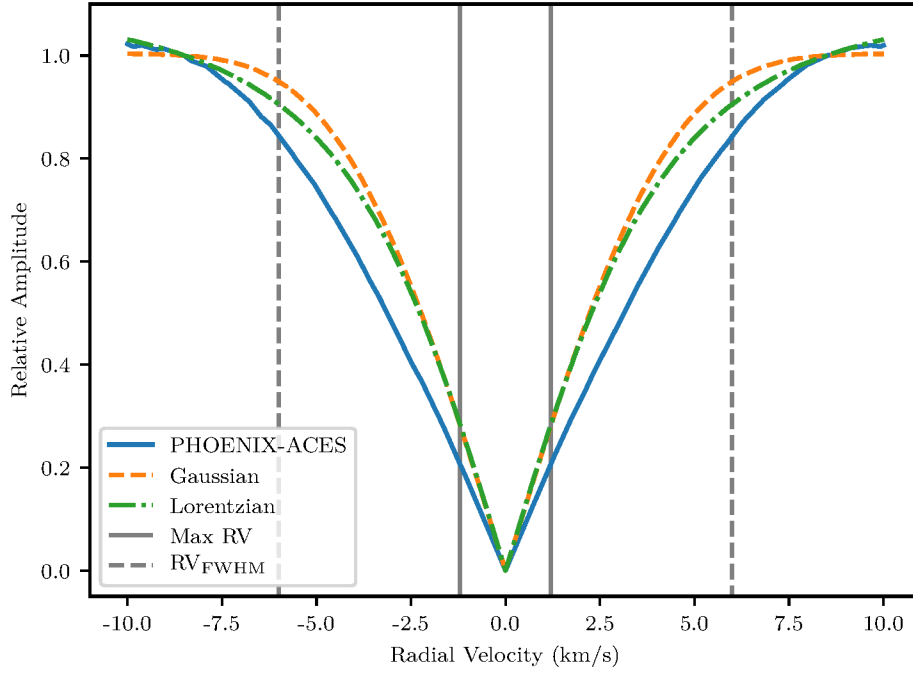


Figure 4.11: Simulated relative amplitude of differential spectra at different companion ΔRV separations revealing the diminished amplitude at very small orbital separations. The solid blue line shows the maximum relative amplitude of the differential signal (from a shifted copy of itself) of a PHOENIX-ACES spectrum with $T_{\text{eff}} = 2500 \text{ K}$, $\text{textrm{logg}}=5.0$, $[\text{Fe}/\text{H}]=0.0$ in the wavelength region 2110–2123 nm. The maximum difference is normalized by the median amplitude between $\pm 7\text{--}10 \text{ km s}^{-1}$, representing a complete line separation. The orange (dashed) and green (dot-dashed) lines represent the relative amplitude of a differential spectrum of a spectrum containing a single Gaussian and single Lorentzian absorption line respectively, each with a unitary amplitude and a $\text{FWHM} = \lambda/R$. The solid vertical lines indicate the estimated companion ΔRV in these observations while the dashed vertical lines indicate the RV corresponding to the FWHM at this wavelength and resolution.

4.5.1.1 Differential scheduling challenges copy from paper

This work has revealed that more care needs to be taken in planning the observations for the spectral differential analysis of faint companions in the future. Paying attention in particular to the FWHM of the lines in the region (governed by resolution and wavelength); the estimated companion ΔRV ; the previous observations from different observing periods; and keeping consistent detector settings.

The original goal for the observations was to obtain two different and “clearly separated radial-velocities” for the secondary companion. However, the program was assigned a low-priority (C, in ESO grading) and, possibly due to operational reasons, the original time requirements necessary to secure well separated RVs for the companion spectra could not be met. This meant that all observations were insufficiently separated to extract a differential spectra for the companion.

The long orbital periods of these targets is also a contributing factor to the insufficient separations. Most of the targets observed here have orbital periods much longer than an observing semester (183 days). An optimal pair of observations (achieved at the extrema) would need to have been obtained from separate observing periods (between 2 months and 19 years apart). In some cases, even observations taken at the beginning and end of a single observing semester would not be sufficient to achieve companion separation (depending on the phase). Requiring separate observing periods to even achieve the minimum ΔRV larger than the line FWHM. At the time it was impossible to ask for time over several semesters in a regular proposal.

Our study demonstrates the importance of proposals for projects that need to be extended over several semesters or years. In the ESO context, this corresponds to “Monitoring proposals” (e.g., ESO, 2017, pg. 18). Observations of the targets explored here, with long orbital periods in particular, would benefit from the ability for multi-period proposals and newer scheduling systems which allow for tighter scheduling constraints, such as a companion RV separation.

For future observations we suggest that the known orbital solution of the companion be used to estimate the companions’ RV curve during the observing period, with the companion $M_2 \sin i$ providing an RV upper-limit. Knowing the instrumental wavelength and resolution, a constraint can then be set to avoid taking observations when the companion spectra are insufficiently separated, or $\Delta RV < \text{FWHM}$. This constraint can be set using the absolute and relative *time-link* constraints available in ESO’s Phase 2 Proposal Preparation (P2PP) tool. Additionally, analysing the known orbital solution beforehand to determine RV constraints will also help identify the best time to observe, if observations from separate periods will be required or, if an optimally separated companion differential is even feasible.

It was unable to be determined if the time differential was asked for in the 2nd proposal round....

CHECK out LOCKWOOD 2014 - maximum likelihood with todcor 1e-4 flux ratio double lined spectra

4.6 Direct recovery in the mIR

It was investigated if this differential technique could be extended into the mid-infrared mIR domain. There were two reasons for this, to develop experience with the mIR domain where the contrast ratios are higher and due to the lack of high-resolution nIR spectrographs available at the time, as CRIRES was being upgraded to CRIRES+.

VISIR is a mIR spectrograph on the VLT, offering diffraction-limited imaging at high sensitivity in three mid-infrared (MIR) atmospheric windows: the *M*-band at 5 μm , the *N*-band between 8–13 μm and

the Q -band between $17 - 20 \mu\text{m}$, respectively. We explored the use of VISIR to detect [a](#) the spectra of Brown Dwarf companions in the mIR. The candidate selected as the best target to investigate was HD 219828 which has a hot-Neptune ($M_2 \sin i = 0.066 M_{\text{Jup}}$) (?) and a recently discovered super Jupiter ($M_2 \sin i = 15.1 M_{\text{Jup}}$) on a long period (13 yr) eccentric orbit ($e = 0.81$)(?).

Based on the spectra of a cool brown dwarfs in the mIR, and the detector configuration available at the time [e](#) the chosen detector settings were the low resolution mode covering the wavelength region $8 - 13 \mu\text{m}$. This wavelength region would have encompassed the NH_4 signature at $10.5 \mu\text{m}$ [and](#) the edge of a CH_4 band at $7.7 \mu\text{m}$, both large features in the BD mIR spectrum.

After performing flux ratio calculations between the host and companion using the ? models and considering the performance of the VISIR instrument and the exposure time calculator it was determined that observations with VISIR to achieve a SNR of 100 were infeasible, requiring 1000's of hours observing time to achieve the necessary signal-to-noise level to separate the companion from a blended spectra. As such the direct separation approach was not continued further in the mIR.

...

This method is very similar to Kostogryz et al. (2013) except that they focus on M-dwarfs host stars with the observations taken at the extrema, in which the companion lines are well separated. [_____](#)

They get a result???

4.7 Summary

This Chapter presented the observations that were gathered having in mind the application of a differential subtraction method (e.g., Ferluga et al., 1997; Kostogryz et al., 2013) to recover the spectra of the faint BD companions. Due to the poorly separated observation times relative to the long orbital periods, the differential subtraction method presented in Section 4.4 was revealed to be inappropriate for these observations as the RV separation of the companion spectra between observations is significantly smaller than the width of individual spectral lines. The small separation of the companion causes the lines of the companion to also mutually cancel, severely reducing the residual signal to well below the available noise level. The requirement of well separated RVs for the companion spectra was clearly stated in the original proposal but was not satisfied by the observations. [The very large orbital periods of some of the targets would not produce a sufficient RV signal during one semester. This was a possible oversight during the proposal stage.](#) The largest estimated companion ΔRV separation between the observations of each target is provided in the 7th column of Table 4.4. [Radial velocity constraints are also valid for](#) other studies such as the detection of reflected light from exoplanets [\(Martins et al. \(2015\)\).](#)

move

Companion Recovery using synthetic models

Because the differential subtraction technique was unsuccessful, not being separable in time. A second method was attempted to try and extract something useful out of the spectra.

We develop this new method, perform some tests and then show the results obtained. There were numerous issues encountered and unsuccessful results.

Contrast our result to other works. More phases, longer integration time, higher SNR.

5.1 Main Section 1

Model fitting two components.

5.2 Binary synthetic spectral recovery

Since the differential method is ineffective for our dataset due to the RV separation between observations, we explored a second approach to detect the presence of the faint companion spectra. This second approach compares the observed spectra to combinations of synthetic spectral models using χ^2 methods which have been extensively used in the literature (e.g., Astudillo-Defru et al., 2015; Passegger et al., 2016; Zechmeister et al., 2018; Nemravová et al., 2016). The temperature of synthetic spectra fitted to the companion will provide some indication of the companions spectral type, but will not produce a direct mass constraint that was the original aim of this work.

5.2.1 Synthetic PHOENIX-ACES models

We use the PHOENIX-ACES (Husser et al., 2013) synthetic spectra library as our reference for the spectral comparison. It uses the most recent version (16) of the PHOENIX code and is suitable for the spectra of cool stars. The full parameter grid space of the PHOENIX-ACES spectra is given in Table 5.1 although we only explore models constrained by the targets explored here.

The spectral model libraries were accessed using the useful “grid tools” interface provided in the *Starfish*¹ Python package (Czekala et al., 2015), which made it efficient to load in the spectra when needed.

¹ <https://github.com/iancze/Starfish>

Table 5.1: Full parameter space of the PHOENIX-ACES spectral grid.

| | Range | Step size |
|----------------------|----------------|-----------|
| T_{eff} [K] | 2 300 – 7 000 | 100 |
| | 7 000 – 12,000 | 200 |
| textrmlogg | 0.0 – +6.0 | 0.5 |
| [Fe/H] | -4.0 – -2.0 | 1.0 |
| | -2.0 – +1.0 | 0.5 |
| α/Fe | -0.2 – +1.2 | 0.2 |

We multiply the synthetic spectra by the wavelength to convert it into photon counts, ignoring multiplicative constants, as done in Figueira et al. (2016)². The spectra were convolved with a Gaussian kernel to match the resolution of the observations ($R = 50\,000$). Due to the distributive property of convolution it is efficient to apply it once to each spectra first, before the spectral pairs are combined.

The PHOENIX-ACES models include dust in equilibrium with the gas phase while ignoring dust opacity and does not include any mixing/settling which is important for cooler BD atmospheres. They set a minimum library $T_{\text{eff}} = 2\,300\text{ K}$ to avoid the temperatures at which the modelling of clouds is necessary. This unfortunately limits the use of this library for this technique to the largest mass companions in our sample. For example a $T_{\text{eff}} = 2\,300\text{ K}$ corresponds to a BD with $M \sim 84M_{\text{Jup}}$ at 5 Gyr from the Baraffe et al. (2003) evolutionary models.

There are other models that extend below 2 300 K such as the BT-Settl models (Allard, 2013; Baraffe et al., 2015). These are discussed in Section ??.

5.2.2 χ^2 method

The well known χ^2 technique measures the weighted sum of the squared deviation between the observation (O_i) and the computed models (C_i), with the minimum χ^2 value representing the best-fit parameters:

$$\chi^2 = \sum_i \frac{(O_i - C_i)^2}{\sigma_i},$$

where σ_i is the error on each measurement. We estimate the σ of each spectrum using the $\beta\sigma$ method (Czesla et al., 2018), using the MAD (median absolute deviation about the median) robust estimator. **This method estimates the spectral noise using numerical derivatives of the spectra. We followed the procedure outlined in Czesla et al. (2018), analyzing the results from successive parameter combinations to settle on an order of approximation (derivative level) of 5, and a jump parameter (pixels skipped to avoid correlations) of 2. We apply the same σ value to all points $\sigma_i = \sigma$. The $\beta\sigma$ method provided σ estimates for the target spectra which correspond inversely to signal-to-noise ratios between 100–500, similar to the values given in Table 4.3 calculated from the continuum of detector 2.**

The computed models are described in Section 5.2.3 and result in a multidimensional grid of χ^2 values for each combination of parameters, namely the spectral temperature, host RV, and companion RV for each detector, observation and target.

We obtain the global minimum of the multidimensional χ^2 -space to represent the best fit to the observed spectra. We sum the multidimensional χ^2 across multiple detectors and determine a global

² Synthetic models provide the spectral energy distribution ($\text{erg s}^{-1} \text{cm}^2 \text{cm}^{-1}$).

minimum χ^2 for the whole observation $\chi_{obs}^2 = \sum_{n=1}^N \chi_n^2$, where N is the number of detectors used. We do not, however, combine the χ^2 values across the separate observations as the RV parameters of the host and companion will vary between each observation. However, since the current observations are insufficiently separated, it may be possible to combine the separate observations; but in general this would not be the case, so was not performed.

The inverse survival function of the χ^2 distribution is used to determine the confidence levels on the minimum χ^2 parameters. The inverse survival function returns a $\Delta\chi^2$ value from the minimum χ^2 value for a given sigma level and degree of freedom³. For example, the $\Delta\chi^2$ for a single degree of freedom required for the 1-, 2-, and 3- σ levels is 1, 4, and 9 respectively (Bevington and Robinson, 2003). This method assumes that the measured flux is observed with a SNR sufficiently high so that the noise on the spectrum is approximately Gaussian, and the χ^2 method appropriate.

For a given observation, the χ_{red}^2 is computed by $\chi_{red}^2 = \chi^2/\nu$ where $\nu = n - m$, the number of observed pixels, n , minus the number of parameters of interest, m ⁴, and is performed after the summation over the detectors.

5.2.3 Computed model spectra

In this section we detail how we transform the synthetic PHOENIX-ACES spectra into the computed models (C_i) to fit to the observations. The spectra have already been converted to the correct unit and resolution.

These synthetic spectra are used individually for the single component model and combined together into a binary model. The results of these models are interpolated to the wavelength grid of the observed spectra and the χ^2 calculated by comparing the model and observation at each point.

5.2.3.1 Single component model

The single model C_i^1 comprises of a single synthetic spectrum, J , (with model parameters T_{eff} , $\log g$, $[\text{Fe}/\text{H}]$, $[\alpha/\text{Fe}]$) and is Doppler shifted by a RV value rv_1 .

$$C_i^1(\lambda) = J(\lambda_0(1 - \frac{rv_1}{c})) \quad (5.1)$$

where λ is the shifted wavelength, λ_0 , the model rest wavelength and, c , the speed of light in a vacuum. The model's flux is then continuum normalized to unity to match the observed spectra, and interpolated to the wavelength grid of the observation.

This single component model analysis is similar to the Passegger et al. (2016) χ^2 fitting. We apply the same re-normalization (see Section 5.2.4) to account for slight differences in the continuum level and possible linear trends between the normalized observation and model. We do not, however, apply any dynamical masking to sensitive lines to make the the χ^2 minima more distinct or linearly interpolate the stellar parameters between the grid models to obtain high precision stellar parameters. This is because we are not trying to derive precise stellar parameters but to detect the spectra of the companions. We

³ In *Python* with the *scipy* package this is a single line `scipy.stats.chi2(dof).isf(1-p)`, where $p = 0.68$ for 1- σ , and `dof` is the degree of freedom.

⁴ $m = 2$ or 4 in the examples explored below

instead include radial velocity components to the χ^2 fitting, which is not included in Passegger et al. (2016).

5.2.3.2 Binary model

In the binary situation we consider the superposition of two synthetic spectral components, one each for the host and companion respectively. Both spectra are Doppler shifted by rv_1 which represents the RV motion of the host star, while the companion spectra is also Doppler shifted by a second RV, rv_2 , representing the RV offset between the host and companion. This choice is arbitrary, but in this way the mean motion of the system relative to Earth is captured only in rv_1 . The two spectra are scaled by their squared radius (see Section 5.2.3.3) then added together, thus fixing the relative amplitude of the two components. Given two spectral components J_1 and J_2 with radii R_1, R_2 this equates to

$$C_i^2(\lambda) = J_1(\lambda_0(1 - \frac{rv_1}{c})) \times R_1^2 + J_2(\lambda_0(1 - \frac{rv_1}{c})(1 - \frac{rv_2}{c})) \times R_2^2 \quad (5.2)$$

The combined spectra is continuum normalized by dividing by an exponential fitted to the continuum of the combined spectrum, as we assume we are in the Rayleigh-Jeans regime. This assumption here is wavelength dependent and other appropriate continuum normalization techniques are also valid. In the case of a BD companion around an FGK star investigated here, the continuum is dominated by the contribution from the host star as it contributes the majority of the spectrum with flux ratios around 2 110–2 160 nm below $\sim 1\%$.

We combine the models in this way to represent the correct absolute flux ratio of the components. The median flux ratio between the two components is calculated for the wavelength range used here as an indication of the flux ratio level.

The binary model should provide meaningful information about the companion parameters (e.g. T_{eff}) and a estimate of the flux ratio of the system. These can be combined with the Baraffe et al. (2003) models to constrain the mass of the companion. However, we need to be careful with this model as the inclusion of extra spectral components and associated parameters could also provide a better fit to observations which do not have a companion, by fitting components of the noise.

The full list of grid parameters for the binary model are $T_{\text{eff}1}$, textrmlogg_1 , $[\text{Fe}/\text{H}]_1$, $[\alpha/\text{Fe}]_1$, rv_1 , $T_{\text{eff}2}$, textrmlogg_2 , $[\text{Fe}/\text{H}]_2$, $[\alpha/\text{Fe}]_2$, rv_2 where the subscripts 1 and 2 indicate the host and companion models respectively.

5.2.3.3 Effective radius

To combine the two synthetic spectra with the correct observed flux ratio we need to integrate the emitted flux over the effective surface area of each emitting body respectively. Ignoring the common multiplicative constants that will disappear with normalization, we scale the two synthetic spectra individually by the square of their respective radii, R_1 and R_2 .

In this work we use the effective radius (PHXREFF keyword) of each component from the PHOENIX model headers. This is the radius used in modelling of the stellar atmospheres. We use this radii as it is directly tied to each model spectrum, and already available. The ratio of the radii from the two synthetic

spectra in the binary models are provided in Table 5.2.

We are aware that using these radii **radii** has its limitations, since as stated previously, there is a degeneracy in BD mass, age, and luminosity of the companion, and in particular a combination of radius-mass and radius-age relationships (Sorahana et al., 2013). Using the PHOENIX-ACES model effective radius does not allow for any independent age constraints to be incorporated, or allow for any variability in the radii to account for uncertainties.

The targets analysed here do not have transits, but if the radius ratio can be independently determined from the photometric transit method (Deeg, 1998) then this could be used to constrain the radius ratio used when combining the binary model spectra instead.

5.2.4 Re-normalization

Slight trends in the continuum level between the observed spectra and computed models were removed using the re-normalization following (Passegger et al., 2016):

$$F_{re-norm}^{obs} = F^{obs} \cdot \frac{\text{continuum fit}_{model}}{\text{continuum fit}_{observations}}. \quad (5.3)$$

The polynomial continuum fits to the normalized observations and models are used to re-normalize the observed spectrum to the continuum of the models. For detectors 1–3 a polynomial of first degree was used, while for detector 4 a quadratic is needed to fit the edge of a strong Hydrogen line (Brackett- γ) at 2166 nm, which lies just off of detector 4. This broad line is only observed in the synthetic spectra and not in the reduced observations. It is assumed that this was normalized out during the reduction process.

For each model we further allow the continuum level to be varied by ± 0.05 as a free parameter taking the model with the smallest χ^2 value.

5.2.5 Reducing parameters

The high dimensionality of the binary model makes it computationally challenging and difficult to analyse the χ^2 space. For reference, the multiplicative parameter space is squared when increasing from one spectral component in the single model to a binary model, and therefore becomes computationally expensive. In general the number of possible parameter combinations for c spectral components each with a grid of m models increases to c^m . If the full set of PHOENIX-ACES library spectra (66456) is explored with a binary fit then this naively balloons to over 4.4 billion possible combinations. Half of these are not unique as the host and companion components are swapped. This is the worst case scenario and we implement a number of assumptions to vastly reduce the parameter-space enabling faster computation.

Our first assumption is to restrict ourselves to models with an Alpha element abundance ($[\alpha/\text{Fe}]$) of zero. This is likely a very good approximation as all our targets have solar metallicity and are thus very likely to belong to the thin disk of the Galaxy, where $[\alpha/\text{Fe}]$ values are close to zero (i.e., solar) – e.g. Adibekyan et al. (2012). Our second is to assume that we can significantly reduce the search space with literature values for the host star. We fix the metallicity of both components to the closest grid to the literature value (usually $[\text{Fe}/\text{H}]=0.00$). We also fix the $\text{textrm{logg}}$ of the host star to its literature values given in Table 4.1. The uncertainties on the literature measurements for $\text{textrm{logg}}$ (~ 0.1) and metallicity (~ 0.05) are both smaller than the grid steps of 0.5 for these parameters. For the $\text{textrm{logg}}$ of the companion we use the Baraffe et al. (2003, 2015) evolutionary model value for the given companions

Table 5.2: Input and recovered parameters on simulations and an observation when applying a single (C^1) and binary (C^2) models. The *textrmlogg* and metallicity were fixed at *textrmlogg*₁ = 4.50, *textrmlogg*₂ = 5.0 and [Fe/H]=0.0 equally for both components. Gaussian noise was added to both simulations with a SNR of 150. Here *m* and *n* are the number of data points and parameters used in each model.

| | Simulation 1 | | | Simulation 2 | | | Observed HD 211847 | | |
|-----------------------|--------------|-----------|---------|--------------|-----------|---------|--------------------|-----------|----------------------|
| | Input | Recovered | | Input | Recovered | | Expected | Recovered | |
| | | C^1 | C^2 | | C^1 | C^2 | | C^1 | C^2 |
| $T_{\text{eff}1}$ | 5 800 | 5 800 | 5 800 | 5 700 | 5 800 | 5 700 | $5\,715 \pm 24$ | 5 900 | 5 800 |
| $T_{\text{eff}2}$ | 4 000 | – | 3 800 | 3 200 | – | 3 100 | $\sim 3\,200$ | – | $>3\,800^{\text{a}}$ |
| rv_1 | 0 | 0.1 | 0 | 6.6 | 6.6 | 6.6 | 6.6 ± 0.3 | 7 | 7.6 |
| rv_2 | 10 | – | 9.8 | 0.5 | – | -1 | 0.5 ± 2 | – | -12.6 |
| R_1/R_2 | 2.57 | – | 2.71 | 3.16 | – | 3.27 | 3.16 | – | $<2.71^{\text{a}}$ |
| F_2/F_1 | 0.084 | – | 0.066 | 0.030 | – | 0.026 | 0.030 | – | $>0.066^{\text{a}}$ |
| m | – | 3 072 | 3 072 | – | 3 072 | 3 072 | – | 2 612 | 2 612 |
| n | – | 2 | 4 | – | 2 | 4 | – | 2 | 4 |
| χ^2 | – | 4 978 | 3 792 | – | 3 746 | 3 630 | – | 37 688 | 33 860 |
| χ_{red}^2 | – | 1.62 | 1.24 | – | 1.22 | 1.18 | – | 21.3 | 19.2 |
| BIC | – | -20 145 | -22 315 | – | -21 477 | -21 377 | – | 18 281 | 14 468 |

^a At the arbitrary upper limit for companion temperature grid (3 800 K).

$M_2/M_2 \sin i$ and hosts age.

We use the estimated companion temperatures from the Baraffe evolutionary models given the companion M_2 or $M_2 \sin i$ and stellar age as a starting point for the companion spectra grid computation and extend the grid in each direction, within the model limits. For example we show the companion temperature grid spanning -600 to $+400$ K in Figure 5.1 and ± 400 K in Figs. 5.2 and 5.3.

The large numbers stated above also do not include the RV grid for each component. The RV grid is user defined and the number of spectra /models to consider increases when the RV grid step size is decreased (finer RV resolution). We can reduce the RV grid space significantly by tailoring it to the target being examined. For each target, we use the estimated RV values from the observation time and orbital parameters, given in Table 4.3 as a centre starting point for the rv_1 and rv_2 values and increment the RV within a few FWHM around those values, or out to the targets K_1 and estimated K_2 values.

An iterative process could be implemented to refine the RV grids, starting at a larger grid with lower RV resolution then performing a higher resolution grid about the minimum χ^2 RV values. This was only done manually but could have been automated. One could expect that a good starting RV grid step be governed by the spectral resolution, e.g. comparable to the FWHM velocity.

For the companions targets with fully resolved orbits the known RV of the host star, rv_1 could also have been fixed. We however left this free to see if the known value would be recovered by the fitting.

Figure 5.1: χ^2 results for companion recovery of a simulated binary observation of a Sun-like star ($T_{\text{eff}1} = 5800$ K) with an M-dwarf companion ($T_{\text{eff}2} = 4000$ K). The top right plot shows the application of a single component model (C^1) while the other three are using a binary model (C^2). Both left hand panels show the distribution of host temperature and host RV. The top right panel shows the distribution for host and companion temperature, and the bottom right the companion temperature and radial velocity. The red circle and yellow star indicate the location of the simulation input and recovered parameters respectively. The white line shows a $3\text{-}\sigma$ confidence level about the minimum χ^2 solution grid point. Each box is centred on the parameter values and shows the grid resolution.

Figure 5.2: Similar to Figure 5.1, χ^2 results for companion recovery of a simulated binary observation similar to HD 211847, ($T_{\text{eff}1} = 5800$ K, $T_{\text{eff}2} = 3200$ K). The top right plot shows the application of a single component model (C^1) while the other three are using a binary model (C^2). Both left hand panels show the distribution of host temperature and host RV. The top right panel shows the distribution for host and companion temperature, and the bottom right the companion temperature and radial velocity. The red circle and yellow star indicate the location of the simulation input and recovered parameters respectively. The white line shows a $3\text{-}\sigma$ confidence level about the minimum χ^2 solution grid point. Each box is centred on the parameter values and shows the grid resolution.

5.3 Results



Here we show the results from applying the companion recovery model to simulated observations and to an observation.

5.3.1 Simulated binaries

To test the companion recovery method we create simulated binary observations using PHOENIX-ACES spectra. White noise was added with a standard deviation $\sigma = 1/\text{SNR}$, for a given signal-to-noise (SNR) level. We then applied the grid-matching recovery technique detailed above and compared the resulting parameters to the inputs.

The results of two example binary simulations are displayed in Figs. 5.1 and 5.2, both simulated with a SNR of 150. The input and recovered parameters for the binary components are indicated by the red circles and yellow stars respectively, and are given in Table 5.2. The $3\text{-}\sigma$ contour is shown in white on the plots to indicate the shape of the confidence level only. The $1\text{-}\sigma$ contours are not shown here as they are much smaller than the temperature grid step and are not easy to visualize at this scale as they are often smaller than the marker shown at the minimum location. Each coloured rectangle is centred on the grid point, with its shape indicating the resolution of the grid space searched.

The first simulation shown in Figure 5.1 is for a Sun-like star with a M-dwarf companion, with a $T_{\text{eff}2} = 4000\text{ K}$. The top-left panel shows the recovered host parameters when the single model is applied to the simulated binary. The top-right and both bottom panels are the parameters recovered when using the binary model. Both left-hand panels display the parameters for the host component to easily compare between models. With both models the host temperature $T_{\text{eff}1}$ is correctly recovered. The host RV, rv_1 , is 0.1 km s^{-1} (two grid spaces) different from the simulated value for the single component model and is correctly recovered with the binary model.

The minimum χ^2 location for the companion temperature is 200 K below the simulated value, and the RV of the companion recovered is 0.2 km s^{-1} below the input value. The input values for the companion are just outside of the $3\text{-}\sigma$ contours shown. The flux ratio for the input is 0.08 while the flux ratio recovered is 0.066 .

The second simulation shown in Figure 5.2 is performed with parameters to mimic the observation of our target with highest flux ratio, HD 211847. In this simulation the single component model recovers a host with the correct RV but a temperature 100 K higher than the input value. Again, adding the companion with the binary model recovers the correct host temperature. The companion temperature recovered is 100 K lower than the input temperature and the RV is different by 2 km s^{-1} which is around one third the FWHM.

In this case with a companion RV offset, rv_2 , near 0 km s^{-1} the host and companion lines are blended. The same spectral lines from both components are trying to match to the same features of the spectra, making it more difficult to recover the companion parameters. In the bottom right panel there appears to be multiple minima for different rv_2 and $T_{\text{eff}2}$ combinations, which we assume is partially due to the small rv_2 .

In both simulations the reduced χ^2_{red} for the binary model is closer to 1. This is not surprising as the binary model contains extra parameters. As mentioned above, we need to be careful, as the extra components from the binary may just happen to fit components of the noise when a binary is not present, or in our case has a low flux ratio. **We analysis the significance between the two models using the “Bayesian Information Criterion” (BIC) (Schwarz, 1978);**

$$BIC = n \ln(m) - 2 \ln(\hat{L}). \quad (5.4)$$

Here n and m are the number of parameters and data points respectively and \hat{L} is the maximum of the Gaussian likely-hood function

$$\hat{L} = \left(\frac{1}{\sigma\sqrt{2\pi}} \right)^m \exp\left(-\frac{\chi^2}{2}\right), \quad (5.5)$$

written in terms of χ^2 and a fixed σ for all data points. The maximum likely-hood of a Gaussian

distribution is equivalent to minimizing the χ^2 . In both simulations $\Delta BIC > 10$ so the preference of the binary model, with the lower BIC value, over the single component model is considered *significant*.

5.3.2 HD211847 observation

HD 211847 is the best candidate for detection as it has a 155 M_J low-mass star companion Moutou et al. (2017). The angular separation of the two bodies is 222 mas (or 11.3 au). Even though it is not a BD it has the highest estimated flux ratio in our sample, of 0.03 based on the Baraffe et al. (2015) evolution models and the known companion mass (see. Table ??). The angular separation of HD211847B is 222 mas with a projected distance of 11.3 au. The result of applying χ^2 fitting to the second observation of HD 211847 is shown in Figure 5.3.

For this target the metallicity of both components was fixed to 0.0 and the $\text{textrm{logg}}$ for the host was fixed at 4.5. The $\text{textrm{logg}}$ for the companion is fixed to 5.0, based on the Baraffe et al. (2015) evolutionary models for the given companion mass and system age. The orbital solution was used to refine the RV search space of both components. The span RV for the companion was extended until a value inside the RV bounds was found.

Again the top left panel of Figure 5.3 shows the recovery with a single component model with the other three for the binary model. The single component model finds a temperature of 5900 K for the host with a rv_1 of 7 km s^{-1} . This is 200 K and 0.4 km s^{-1} different above the expected parameters. The binary model finds a host temperature of 5800 K, which is the second closest model to the literature value, $>100 \text{ K}$ different. The host RV value recovered with the binary model is 7.6 km s^{-1} , which is 1 km s^{-1} higher than expected. For the single component model there is a barely noticeable secondary minima near this 7.6 km s^{-1} RV value recovered by the binary model. Again these RV differences are smaller than the FWHM of the lines. The $3\text{-}\sigma$ contour is small, just visible on the right hand side of the star in the bottom left panel, and hidden behind the markers in the other panels.

For the companion in the binary model, on the right side of Figure 5.3, the minimum χ^2 for the companion temperature is at the upper temperature limit of the grid shown. If we extend the grid of companion temperature towards higher temperatures the best fit location continues to increase in temperature, continually hitting the upper limit until it is close to the host temperature, $>2000 \text{ K}$ above the expected companion temperature. When the companion temperature becomes this high it also affects the recovered parameters for the host star to offset the features of the brighter companion.

The χ^2_{red} values for the single and binary models are 21 and 19 respectively, far from 1, indicating that both models are a poor fit to the observations. The $\Delta BIC = 3812 > 10$ indicating that binary model is still preferred. We plot the binary model for the best fit solution alongside the observed spectra in Figure 5.4. We see that there is a large spectral mismatch between the synthetic models and the observation. Extra wavelength masking was applied to many of the largest mismatched synthetic lines to remove their influence. The grey areas mark regions which have been masked out, either from the centres of deep telluric lines (the thin masks matching spectral gaps), or the more prominent mismatched lines in the synthetic spectrum excluded from the χ^2 analysis. One clear example of a mismatched line is a synthetic line at 2132.5 nm that is clearly not observed in detector 2 (top right). Even with the majority of the mismatched lines removed the detection of the companion was still unsuccessful.

For detectors 1 and 2 it appears that the synthetic spectra contain many more deeper lines than observed. For detector 3 the red half of the detector was masked out as there appears to be an offset between the observed lines. With 3–4 lines that appear to be consistently offset from the observation it

Figure 5.3: χ^2 result grid for observation 2 of HD 211847, similar to Figs. 5.1 and 5.2. The top right plot shows the application of a single component model (C^1) while the other three are using a binary model (C^2). Both left hand panels show the distribution of host temperature and host RV. The top right panel shows the distribution for host and companion temperature, and the bottom right the companion temperature and radial velocity. The red circles indicate the literature values or calculated parameters for the target while the yellow star indicates the minimum χ^2 solution. The error bar on the $T_{\text{eff}1}$ is from the literature while the error bars on rv_1 and rv_2 are calculated by propagating the orbital parameter uncertainties through the radial velocity equation. The white line shows a $3\text{-}\sigma$ confidence level about the minimum χ^2 solution grid point, not always visible here due to the large χ^2 values.

could be a wavelength calibration issue, although the telluric lines appear to be sufficiently corrected in this region, attesting for the quality of the wavelength calibration, and making it incompatible with the offset. For detector 4 the observed lines do not agree at all with the models. With many observed lines not in the model and only one line with some agreement in wavelength, detector 4 is masked out completely and not used in the χ^2 fit. Individual inspection of the χ^2 results for each detector also revealed that there was a large discrepancy between the 4th detector and the other three, with a different RV value for the host star and a χ^2 values an order of magnitude higher. The edge of a deep Hydrogen line (Brackett- γ) off the edge of the detector 4 is also clearly seen in the continuum of the model $>2162\text{ nm}$.

We applied this same method to the remaining targets, with similar results. In brief, we conclude that the companion spectra cannot be correctly detected in our data using this method.



5.3.3 Companion injection-recovery

To determine the detection limits for this method we employ an injection-recovery approach. We take the observed spectra and inject onto them a synthetic companion, at the absolute flux ratio to which it

Figure 5.4: Comparison between the observed HD 211847 spectrum (blue) and the best fit synthetic binary model (orange dashed) for each detector. The bottom section of each panel shows the residuals between the parts of the observation used in the χ^2 fit and recovered binary model ($O - C^2$) in purple. The red dashed line shows the difference between the recovered binary model and the binary model with the exact same parameters except for the estimated companion temperature of 3 200 K ($C^2[3200 \text{ K}] - C^2$). The grey shading indicated the wavelength regions where masking has been applied. The thinner masked regions that match with cuts in the observed spectra are where the centres of deep ($>5\%$) telluric lines that have been masked out are.

would have been added to a synthetic host with the same parameters. The injected companion RV is set to 100 km s^{-1} so that the companion lines are well separated from the lines of the host. This separation chosen is slightly larger than what we have with our observations, rv_2 given in Table 4.3.

We restrict the search space by fixing the host parameters $T_{\text{eff}1}$ and $\text{textrm{logg}}_1$ to those recovered fitting the non-injected spectra by a single component model. The wavelength masking is used to reduce the level of mismatch between synthetic and observed spectra.

We apply the recovery method developed above on the injected spectrum, leaving only the companion $T_{\text{eff}2}$ and rv_2 parameters free, to recover the injected companion. We repeated this for injected companions with temperatures below 5 000 K.

We also perform the injection-recovery with synthetic host spectra, representing each target. The wavelength range of the synthetic spectra used for this is three sections interpolated to 1 024 values in the wavelength span of detectors 1, 2, and 3. For each section, Gaussian noise is added at the level measured in the corresponding detector for the in the observation of the target being represented.

In Figure 5.5 we show the results of the injection-recovery on HD 30501. The blue dots represent the recovered companion temperature when injected into real observations, while the orange triangles represent injection into a synthetic host. Error bars of $\pm 100 \text{ K}$ are included to indicate the grid size, and do not come from the recovery itself. The black dashed diagonal is the temperature 1:1 relation, where a correctly recovered companion should lie.

The grey shaded region indicates the $\pm 1 000 \text{ K}$ temperature range explored for the injection-recovery of the companion. This shows how the bounds of the grid are recovered at low temperatures.

For HD 30501 the injection onto synthetic and observed spectra produce similar results. At temperatures above 3 800 K in both the real and synthetic the injected companion is recovered within 100 K. For injected companion temperatures below 3 800 K the temperature recovered is systematically higher than the injected value. This indicates that the companion is not correctly recovered and is affected by the added noise. We determine this temperature to be the upper temperature limit for the recovery. For the other stars we could not conclude on the upper limit due to spectral mismatch issues. In these cases we use the results from the synthetic injection to derive a temperature recovery cut-off for each target, each simulated with the closest host star spectrum.

In Figure 5.6 we show the minimum χ^2 for each companion temperature in the recovery grid. We do this for 7 different injected companion temperatures between 2 500 and 4 500 K. For the higher temperature companions, the χ^2 is parabolic in shape, recovering the correct temperature, as expected. At lower temperatures there is a strong asymmetry in the χ^2 with it flattening out on the lower temperature side. The 1-, 2-, 3- σ values (with 2 degrees of freedom) of 2, 6 and 11 above the minimum χ^2 are not shown in the bottom panel of Figure 5.6 which is a close-up around the minimum χ^2 as are indistinguishable in

Figure 5.5: Result of simulated injection-recovery of synthetic companions on HD 30501. The blue dots and orange triangles indicate the recovered companion temperature for the observed and synthetic spectra respectively. The ± 100 K error bars are the grid step of the synthetic models. The black dashed diagonal shows the 1:1 temperature relation. The grey shaded region indicates the ± 1000 K temperature range explored. Gaussian noise added to the synthetic spectra was derived from the observed spectra.

Figure 5.6: (top) Companion temperature verses χ^2 for simulations with different injected companion temperatures. Other fixed parameters for these fully synthetic simulations was $T_{\text{eff}1} = 5200$ K, $\log g_1 = 4.5$, $\log g_2 = 5.0$, and both $[\text{Fe}/\text{H}] = 0.0$. A fixed Gaussian noise corresponding to a SNR of 300 was used. (bottom) A close up view of $\chi^2 < 15$. The three horizontal grey lines indicate the 1, 2, 3 **sigma** with 2 degrees of freedom. The vertical dotted lines indicate the location of the minimum χ^2 recovered for each companion. The black solid vertical in both panels shows the 2300 K cut-off of the PHOENIX-ACES models

the top panel due to the χ^2 y-scale. The black vertical line indicates the 2300 K temperature limit of the PHOENIX-ACES models.



Using the temperature cut-off values, we derive an upper mass limit for the companions around our stars using the Baraffe et al. (2015) evolutionary models, finding the closest point matching the spectral temperature cut-off and $\text{textrm{logg}} = 5.0$. These values are given in Table 5.3 and are between 560 and 618 M_{Jup} . The flux ratio between the cut-off and the host star are also provided for, being between 5 and 15% in this wavelength span.

Hoeijmakers et al. (2015) Context. The spectral signature of an exoplanet can be separated from the spectrum of its host star using high-resolution spectroscopy. During these observations, the radial component of the planet's orbital velocity changes, resulting in a significant Doppler shift that allows its spectral features to be extracted.

Aims: In this work, we aim to detect TiO in the optical transmission spectrum of HD 209458b. Gaseous

Table 5.3: Upper mass limits of target companions assuming a companion $\text{textrm{logg}}=5.0$. Masses are derived from Baraffe et al. (2015) evolutionary models using T_{eff} and $\text{textrm{logg}}$. The flux ratio F_2/F_1 is the absolute flux ratio between the cut-off temperature and the target host star.

| Target | T_{eff} cut-off (K) | F_2/F_1 | Mass limit (M_{Jup}) |
|-----------|------------------------------|-----------|---------------------------------|
| HD 4747 | 3 900 | 0.084 | 598 |
| HD 162020 | 3 900 | 0.147 | 598 |
| HD 167665 | 3 800 | 0.054 | 560 |
| HD 168443 | 4 000 | 0.094 | 618 |
| HD 202206 | 3 900 | 0.075 | 598 |
| HD 211847 | 3 900 | 0.079 | 598 |
| HD 30501 | 3 800 ^a | 0.106 | 560 |

^a From observed spectra

TiO has been suggested as the cause of the thermal inversion layer invoked to explain the dayside spectrum of this planet.

Methods: We used archival data from the 8.2 m Subaru telescope taken with the High Dispersion Spectrograph of a transit of HD 209458b in 2002. We created model transmission spectra that include absorption by TiO, and cross-correlated them with the residual spectral data after removal of the dominating stellar absorption features. We subsequently co-added the correlation signal in time, taking the change in Doppler shift due to the orbit of the planet into account.

Results: We detect no significant cross-correlation signal due to TiO, though artificial injection of our template spectra into the data indicates a sensitivity down to a volume-mixing ratio of $\sim 10^{-10}$. However, cross-correlating the template spectra with a HARPS spectrum of Barnard’s star yields only a weak wavelength-dependent correlation, even though Barnard’s star is an M4V dwarf that exhibits clear TiO absorption. We infer that the TiO line list poorly matches the real positions of TiO lines at spectral resolutions of $\sim 100\,000$. Similar line lists are also used in the PHOENIX and Kurucz stellar atmosphere suites and we show that their synthetic M-dwarf spectra also correlate poorly with the HARPS spectra of Barnard’s star and five other M dwarfs. We conclude that the lack of an accurate TiO line list is currently critically hampering this high-resolution retrieval technique.,

5.3.4 Junk from paper about BT-settl

Alot of this section needs to be cut out, lots of repeats and it is not well structured. Basically it will say there is this other model that is better for BDs as it differs “like this” but Fig. ref fig:hd211847-models show that it will also have strong mismatch to make it difficult to recover.

The BT-Settl (allard et al 2009, 2010 2011 2012 baraffe2015) models, a different flavour of Phoenix models, are more suitable for BD atmospheres as they include the formation of dust/cloud and hydrodynamical modelling atmospheric mixing/settling for atmospheres with T_{eff} below ~ 2600 K. These are valid across the regime from stars to BDs as cool as 400 K. The PHOENIX-ACES models completely avoid the modelling of clouds and settling by the lower temperature restriction of 2 300 K.

The PHOENIX-ACES models dust in equilibrium with the gas phase but ignores the dust opacity and

does not include any settling. It does however include a new Astrophysical Chemical Equilibrium Solver (ACES, Barman 2012); adds parametrisations for the mass and mixing-length; and uses the Asplund et al. (2009) solar abundances. All these modifications together make it difficult to quantify the spectral changes from each individual change.

The two of the recent “flavors” are the BT-Settl (Allard et al., 2010; Baraffe et al., 2015) and the PHOENIX-ACES (Husser et al., 2013) which use versions 15.5 and 16 of the PHOENIX code respectively.

Even though the BT-Settl models are more suited for the entire range of BD temperatures, we restrict ourselves to the PHOENIX-ACES synthetic spectra for a number of reasons. The ease of use and availability from the spectral library webpage⁵. The ease of use using the Starfish tools, a wide parameter range and fairly consistent parameter grid span, and the effective radius of the modelled star provided in the fits header.

These were not used in this instance for a couple of reasons, the ineffectiveness to produce a reliable detection on the observations using PHOENIX ACES spectra for our largest companions, which fall well within the PHOENIX ACES temperature limit.

The PHOENIX-ACES models also provide dimensions of effective radius of the star, in the header. This is required for the method presented here as we need to scale the spectra by their respective surface area when combining together. This PHOENIX-ACES lower temperature limit restricts its use to only the higher mass BD companions in our sample ($> 0.08M_{\odot}$ at 5 Gyr from the Baraffe et al. (2003) models).

The most recent BT-Settl spectral library designated CIFIST2011_2015⁶ (Baraffe et al., 2015) is only available for $1\,200\text{--}7\,000\text{ K}$ $\text{texp}=\log=2.5$ to 5.5 and a fixed metallicity and alpha of 0 and includes newer Caffau et al. (2011) solar abundances.

The newer PHOENIX-ACES models are limited to $T_{\text{eff}} > 2\,300\text{ K}$ which only cover the larger BDs. To evaluate the lower mass BDs we use the **other model**, more suitable for cooler BDs and low mass star as they incorporate modeling of dust, clouds etc. . .

The spectral model libraries were accessed using the useful “grid tools” provided in the Starfish⁷ Python package (Czekala et al., 2015).

Both sets of synthetic models do not handle the affects of radiation from a neighbouring star, which may have an affect on the binary orbits here.

PHOENIX-ACES models dust in equilibrium with gas phase but ignores the dust opacity and does not include any mixing/settling in cooler atmospheres. This is avoided by having a minimum library $T_{\text{eff}} = 2\,300\text{ K}$. This unfortunately limits the use of this library for this technique to the larger mass companions in our sample. For example a $T_{\text{eff}} = 2\,300\text{ K}$ corresponds to a BD with $M \sim 0.08M_{\odot}$ at 5 Gyr from the Baraffe et al. (2003) evolutionary models.

Even though the BT-Settl models are more suited for the entire range of BD temperatures down to 400 K, through hydrodynamically modeling the mixing and settling of dust/clouds, we restrict ourselves to the PHOENIX-ACES synthetic spectra in this work for a number of reasons. The ease of use and availability from the spectral library webpage⁸. The effective radius of the modelled star are provided in the fits header and required for the calculation of the flux ratio.

The most recent BT-Settl spectral library designated CIFIST2011_2015⁹ (Baraffe et al., 2015) is

⁵ http://phoenix.astro.physik.uni-goettingen.de/?page_id=15

⁶ https://phoenix.ens-lyon.fr/Grids/{BT-Settl}/CIFIST2011_2015/

⁷ <https://github.com/iancze/Starfish>

⁸ http://phoenix.astro.physik.uni-goettingen.de/?page_id=15

⁹ https://phoenix.ens-lyon.fr/Grids/{BT-Settl}/CIFIST2011_2015/

only available for 1200-7000 K $\text{textrm{logg}}=2.5$ to 5.5 and a fixed metallicity and α of 0 and includes newer Caffau et al. (2011) solar abundances.

The BT-Settl grids were harder to obtain and use.

As we do not recover suitable results for HD211847 which is supposed to have a temperature around 3400 K we suspect that it is not possible for lower temperature either so don't try to extend to the BT-Settl models.

PHOENIX ACES defines grid as T_{eff} , $\text{textrm{logg}}$ and Mass which can then be used to determine Radii. See (Husser et al., 2013) section 2.3.1 Mass.

Both BT-Settl and aces are spherical ...

5.3.5 Incremental changes

incremental changes in models are small

We took the synthetic models and investigated how the synthetic binary changed as the model parameters were incremented. For the temperature of the companion to be incremented by 100 K this resulted in change to the spectrum with a std of XXX. This is around a SNR of around 500. The change in the models with incremental changes in temperature is small, Changes in log and feh are larger but we fixed these for the application above.

5.3.6 Note about a target - discussion of results

Another example is HD 162020, which has the lowest orbital period (8.4 days) of our targets. It should have been possible to obtain an optimal pair of observations in one semester, but the second observation was taken immediately following the first. This means that the $\delta RV = 0.363 \text{ km s}^{-1}$ between the two observations, is comparable to the ΔRV that occurs during each individual observation. With tighter scheduling restrictions this target could have been observed with the optimal RV separation at the extrema of $\Delta RV = 2K_2$). Whether the flux ratio of $7e^{-6}$ for this target and the interaction of different spectral lines would have made it possible to recover companion mass is a separate issue.

5.3.6.1 Wavelength range

The wavelength choice for the spectra analysed here, observed with the intention to apply the spectral differential technique, was selected due to the location of the K -band telluric absorption window. This wavelength range, with a narrow wavelength range $\sim 50 \text{ nm}$ set by the CRIRES instrument. This wavelength range is likely not the best choice for the proposed study. may contribute to the poor results from the companion recovery technique.

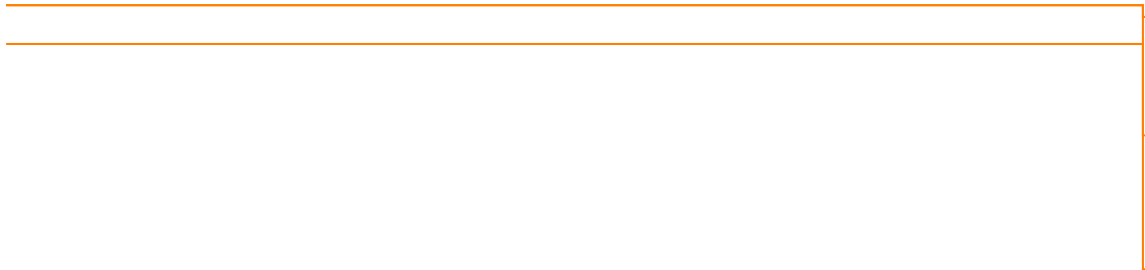
For instance Passegger et al. (2016) used four different spectral regions for the precise parameter determination of M-dwarfs. Specific lines from the different wavelength regions are affected differently by the model parameters: T_{eff} , $\text{textrm{logg}}$, and $[\text{Fe}/\text{H}]$; and are used to break degeneracies in the PHOENIX-ACES parameter space.

Changing the wavelength coverage to regions with lines sensitive to stellar parameters for both stars and BDs, as well as using a larger wavelength range that will be achieved by CRIRES+, may help to improve the recovery results of the companion recovery technique presented here. We note that if the wavelength range is increased by taking separate observations at different wavelengths, not covered

finish this line

by a single exposure, then changes in the RV of both components between the different wavelength observations may need to be accounted for.

Try some Cross-correlations on simulations.



Chapter 6

Information content of nIR Spectra

The work presented in this chapter focuses on calculating and analysing the information content of stellar spectra, specifically the radial velocity precision in the nIR. It is very different from the previous chapters in which the detection of the companions spectra was attempted.

this doesn't seem right

The field of exoplanet detection in the nIR is expanding with several new high resolution nIR spectrographs available in the near future. For instance CARMENES is already performing observations while SPIRou, NIRPS, and CRIRES+ are near completion. One science objective common to all four instruments is the detection of small mass planets around M-dwarf stars utilizing the radial velocity technique. The fundamental radial velocity precision of M-dwarf spectra attainable at different wavelength regions calculated in Figueira et al. (2016) was used to influence some design choices of SPIRou, NIRPS specifically.

The purpose of the work presented in this chapter is to extend the work of Figueira et al. (2016), computing the theoretical RV precision of stellar spectra over a wider range of situations. An investigation into the effect of teff and $[\text{Fe}/\text{H}]$ on precision is performed and a comparison of RV precision of the recently observed nIR M-dwarf spectra from CARMENES library and their synthetic counterparts will be performed. This is to test how the RV precision of synthetic models compares to reality. The aim is to compare the fundamental precision of nIR spectra to the synthetic models, to

6.1 Overview

The pursuit of detecting exoplanets, especially “habitable” and “Earth-like” planets, requires state-of-the-art instrumentation with high precision. One of the key detection methods, the Radial Velocity (RV) method, measures the wobble induced on the Star by the planet as they orbit their common barycentre.

rv method

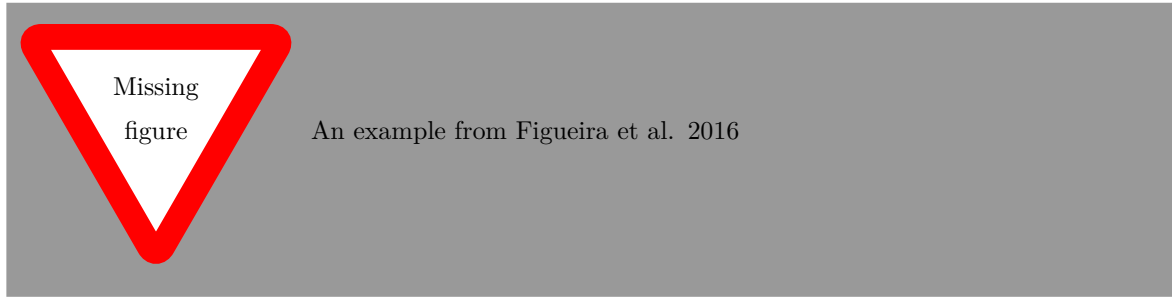
add Some stuff about mass and period from Pedros paper

put in introduction??

An increase in the number of nIR spectrographs is increasing to focus on cooler M-dwarfs stars which have a easier* chance of detecting Earth-like planets in the habitable zone. SPIRou, NIRPS and CARMENES. Also CRIRES+. . . This work continues the assessment of RV precision levels possible in this domain. A more precise measurement can be achieved from X band then the Y-band. . . or in order XYZ of precision.

Check mission statements for these

For example from Figueira 2016 see figure



This work is not directly related to detecting exoplanet atmospheres themselves but investigates the theoretical and observed RV precision of M-dwarf spectra in the nIR. This has previously helped the aid the direction of instrument design by identifying the wavelength regions with the best RV precision (Figueira et al., 2016) but can also help in the planning of observations, by understanding how the precision changes with spectral type and observed SNR. This can help in detecting the presence of “habitable Earth-like” planets around M-dwarfs which will likely have their atmospheres eventually probed.

6.2 Radial velocity precision

The first detections of extrasolar planets with the RV technique were hot-Jupiters; Jupiter mass planets in close orbits to their star. The RV precision required to detect the first hot-Jupiter, 51 Peg b, was Mayor and Queloz (1995) using Since that time the instrumental development and the detection and observation technique refined to achieve RV precisions better than 1 m s^{-1} . The recently commissioned ESPRESSO optical spectrograph is designed with the goal of achieving 10 cm s^{-1} . The level of precision required to detect an Earth mass planet in an 1 year orbit round a Sun-like star.

find mayor
queloz preci-
sion achieved
what reference

Over the years the community has pushed the limits of this technique to smaller and smaller planetary masses. An example is shown in Figure 6.1.

RV amplitude scales with mass of the star $M_{\star}^{-2/3}$ and with the planetary orbital period $P_{\text{orb}}^{-2/3}$.

The detection of an Earth-mass planet inside the habitable zone around a solar-type star, the RV amplitude is 10 cm s^{-1} . If that a planet with the same characteristics is instead orbiting a M-dwarf, the RV amplitude is larger than 1 m s^{-1} . This is due to two factors, the smaller mass of the host star, and the closer habitable zone, due to a lower luminosity output of the host.

Artigau et al. (2018) recently compared archival spectra of Barnard’s Star, an M-dwarf, and found that state-of-the-art atmosphere models over-predict the *Y*- and *J*-band RV content by more than a factor of ~ 2 , while under-predicting the *H* and *K*-band content by half. in this work we find similar?

We are currently aiming to extend this work over the whole M-dwarf range, from M0-M9.

History of Precision calculations: Connes 1985 - Bouchy et al. 2001 - photon noise limit on rv measurements. Figueira et al. (2016) - focus on M-dwarfs parameter range to specify new instrumentation windows to focus. Reiners 2017 - CARMENES sample. Some precision pedros school section other precision source $r^{1.5}$

History of Pre-
cision calcula-
tions

6.2.1 Fundamental photon noise limitation

A technique to calculate the theoretical radial velocity precision of a spectrum using the full spectral information in an optimal way was presented by Connes (1985). Here we provide the radial velocity